Hindawi
Geofluids
Volume 2019, Article ID 5210404, 23 pages
https://doi.org/10.1155/2019/5210404

Research Article

Creation of Secondary Porosity in Dolostones by Upwelling Basement Water in the Foreland of the Alpine Orogen

Lukas Aschwanden,[1] **Larryn W. Diamond**,[1] **Martin Mazurek**,[1] **and Donald W. Davis**[2]

[1]*Institute of Geological Sciences, University of Bern, Baltzerstrasse 3, CH-3012 Bern, Switzerland*
[2]*Department of Earth Sciences, University of Toronto, 22 Russell Street, Toronto, Canada M5S 3B1*

Correspondence should be addressed to Lukas Aschwanden; lukas.aschwanden@geo.unibe.ch

Received 22 September 2018; Accepted 27 November 2018; Published 24 March 2019

Academic Editor: Jean-Luc Michelot

Creation of secondary dissolution porosity in carbonate rocks during deep burial has the potential to improve reservoir properties for hydrocarbons, gas storage, and geothermal applications. However, the occurrence and mechanisms of such porosity enhancement are controversial. Here, we present compelling evidence for generation of deep burial porosity from the Swiss Molasse Basin, where dissolution of eogenetic anhydrite nodules in dolostones of the Middle Triassic Muschelkalk increased the matrix porosity by up to 15 vol.%. We reconstruct the genesis and evolution of the anhydrite-dissolution porosity based on petrography, porosity determinations, analyses of stable and radiogenic isotopes (δ^2H, δ^{18}O, δ^{34}S, and ^{87}Sr/^{86}Sr), fluid inclusion studies, and laser U–Pb geochronology of secondary calcite. The results show that modified meteoric waters derived from the Variscan crystalline basement ascended via basement–cover cross-formational faults into the overlying Muschelkalk, where they dissolved the anhydrite nodules throughout an area of at least 55 km^2 at 700–2300 m depth and 40–160°C. Secondary calcite in anhydrite moulds yields Late Eocene to Middle Miocene U–Pb ages, which coincide with the timing of basement uplift in the foreland bulge of the Swiss Alpine Orogen. This uplift provided the hydraulic gradients to drive meteoric water deep into the adjacent Molasse basin. Similar enhancement of reservoir properties can be expected in dolostones in other foreland basins that are bordered by a foreland bulge in which fractured basement rocks are exhumed.

1. Introduction

Carbonate rocks are being investigated worldwide owing to their economic importance as hydrocarbon reservoirs, as potential storage sites for injected gases (seasonal methane and anthropogenic CO_2) and as sources of geothermal heat. However, prediction of their porosity at depth is difficult because it depends on many factors, such as primary features inherited from a variety of possible depositional environments, as well as features due to any of various eo-, meso-, and telogenetic modifications that either reduce porosity or create new, secondary porosity by carbonate dissolution. Such secondary dissolution porosity is of great interest for exploration as it has the potential to significantly increase the storage capacity and permeability of carbonate reservoirs. The development of secondary dissolution porosity has been traditionally ascribed to early, near-surface diagenetic processes, commonly those tied to subaerial exposure and infiltration of freshwater, for example [1, 2]. More recent studies claim that significant volumes of pore space can be created by dissolution of carbonate during deep burial [3–6] (and other references reviewed by Ehrenberg et al. [7]). However, Ehrenberg et al. [7] argue that the model of carbonate dissolution during deep burial lacks a rigorous observational basis and that it is inconsistent with solubility constraints.

In contrast, dissolution of calcium sulphate (gypsum or anhydrite) within carbonate rocks is a process cited by Ehrenberg et al. [7] that could create significant porosity during burial but that has received almost no attention in the literature. Here, we present an instructive case of this process from the Middle Triassic Muschelkalk in the Swiss Molasse Basin, in which dissolution of eogenetic anhydrite nodules has notably increased the porosity of the dolostone

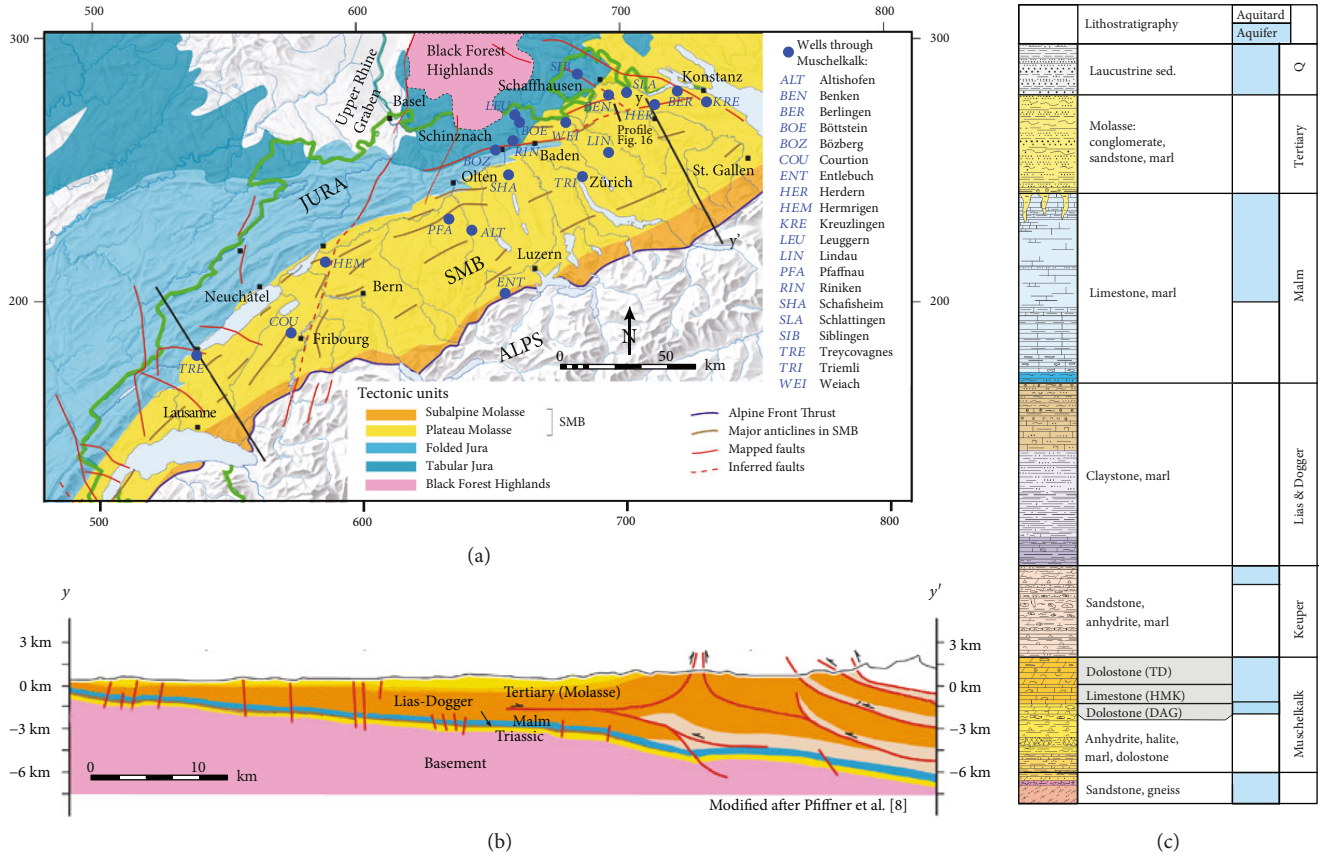

Figure 1: (a) Geology of the Swiss Molasse Basin. The thick green line is the national border. Coordinates are Swiss km grid. (b) Cross section y–y' after Pfiffner et al. [8]. (c) Litho- and hydrostratigraphy of the Mesozoic and Cenozoic sediments at the Benken (BEN) well (TD: Trigonodus Dolomit; HMK: Hautpmuschelkalk; DAG: Dolomit der Anhydritgruppe; modified after Nagra [9]).

matrix. We reconstruct the genesis and evolution of the secondary porosity based on analyses of pore-filling minerals in drill core samples, including petrography, analyses of stable and radiogenic isotopes (i.e., δ^2H, δ^{18}O, δ^{34}S, and ^{87}Sr/^{86}Sr), fluid inclusion studies, and U-Pb geochronology. The results tightly constrain the provenance and age of the anhydrite-dissolving solutions. When interpreted within the framework of existing knowledge on the burial history and hydrogeological evolution of the Muschelkalk rocks, all these new observations lead to a consistent explanation of the origin and geographical distribution of the anhydrite-dissolution porosity, and they provide compelling evidence for the generation of porosity in dolostones during deep burial.

2. Geological Setting

2.1. Geology of the Swiss Molasse Basin (SMB). The Muschelkalk dolostones are part of the Mesozoic sediment stack covering the pre-Alpine crystalline basement in the Swiss Molasse Basin (SMB), the foreland trough of the Alpine orogeny (Figure 1(a)). The basement includes Variscan granites and polymetamorphic gneisses as well as troughs of Permocarboniferous terrestrial sedimentary rocks, all capped by a thin sandstone (Buntsandstein) formed by erosion of the basement rocks in the Early Triassic. The Mesozoic cover comprises a sequence of Triassic–Cretaceous sediments that dip beneath a wedge of Cenozoic Molasse deposits at an angle of approximately 3–5° towards the SE (Figure 1(b)). Thus, the top of the Muschelkalk is exposed along the northern margin of the SMB but it reaches over 5000 m depth in the SE beneath the Alpine Front.

The Muschelkalk is known for its regional aquifer properties, which are largely due to the matrix porosity and permeability of two dolostone subunits, the Trigonodus Dolomit and the Dolomit der Anhydritgruppe [10]. Our investigations focus on the northeastern part of the Swiss Molasse Basin where the anhydrite-dissolution porosity has been observed in drill core and where the density of wells and thus information on the dolostones is highest (Figure 1(a)). There, the Trigonodus Dolomit (TD) is 12–42 m thick and lies at depths of 60–2270 m. Below this unit is the 24–46 m thick Hauptmuschelkalk (HMK) (Figure 1(c)), a series of low-porosity, low-permeability, partly dolomitized limestones, followed below by the Dolomit der Anhydritgruppe (DAG), which is 7–17 m thick and lies at depths of 136–2300 m (Table A.1). This package of two dolostones and their intervening limestones is sandwiched between thick sequences of impermeable evaporites: the Sulfatschichten below (~50 m thick, containing anhydrite

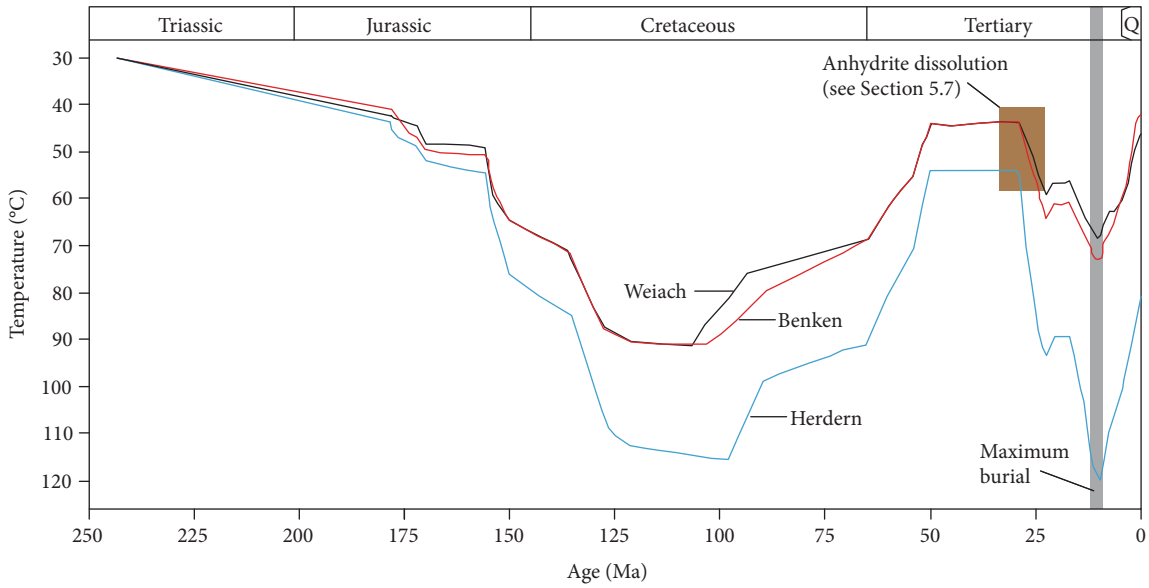

Figure 2: Reconstructed temperature evolution at the top of the Trigonodus Dolomit in the NE part of the SMB, based on data in Nagra [9].

and halite) and by the Gipskeuper above (~70 m thick, containing anhydrite). Further above lie the clay-rich aquitard sequences of the Jurassic (~300 m thick; Figure 1(c)).

2.2. Burial History. The burial and thermal history of NE Switzerland is rather complex (Figure 2). The Mesozoic–Early Cenozoic period (~252–66 Ma) was characterized by regional subsidence with little tectonic activity. However, from the late Cretaceous onwards, NW–SE-directed crustal shortening inverted the basin and culminated in the Eocene collision of the European and Adriatic continents and the development of the Alpine orogen [11]. Flexural loading by the Alps induced a second stage of subsidence of the North Alpine Foreland during Oligocene–Middle Miocene times (~34–10 Ma), and shallow-marine and continental Molasse sediments were deposited within the developing basin [12]. Maximum burial occurred at around 10 Ma [13] (Figure 2; [9]).

Importantly for the hydrogeological development of the SMB, this foreland subsidence was accompanied by uplift along its northern margin in the area of the future Black Forest Highlands (Figures 1(a) and 3). The early stage of this process occurred during the Late Eocene–Oligocene (~38–23 Ma) and amounted to only a few hundreds of meters of uplift as shoulder horsts, concurrent with subsidence and rifting along the Upper Rhine Graben situated to the west of the Black Forest Highlands (Figure 1(a)). More extensive uplift of the Black Forest Highlands began during Middle Miocene times (~14 Ma), eventually resulting in the erosional exposure of the Variscan gneiss basement and regional tilting of the flanking cover strata towards the SSE [12] (Figures 1 and 3(c)). The extensional tectonic regime in the upper crust reactivated numerous faults and formed flexures in the SMB, primarily oriented along old Paleozoic structures in the basement [12, 14, 15].

2.3. Hydrogeological Evolution. The Muschelkalk unit was deposited during Early Anisian–Early Ladinian times in shallow marine, partly lagoonal and intertidal settings [16, 17]. Dolomitization to form the Trigonodus Dolomit and its anhydrite nodules occurred soon after deposition via mixing of refluxing evaporative brine with meteoric runoff from the Variscan granite-gneiss hinterland [18] (some of the same types of Variscan rocks occur today in the Black Forest Highlands and in the basement of the SMB). The runoff had become saline through interaction with near-shore sabkhas prior to laterally infiltrating the marine sediments. The Dolomit der Anhydritgruppe, on the other hand, formed directly in a sabkha environment. Therefore, during subsequent burial of the dolostones through to at least the Paleogene (Figure 2), the residual pore water in both dolostones would have been a Ca–Na–Cl brine of >20 wt.% salinity, in equilibrium with anhydrite. It is less certain what the $\delta^{18}O$ values of the pore waters would have been, but presumably they were similar to modern sabkha fluids between 3 and 8‰ VSMOW [19].

In contrast to the residual dolomitizing fluid, the present-day groundwater in the Upper Muschelkalk at the shallow northern margin of the SMB has low salinities (<0.2 wt.%) and low $\delta^{18}O$ values of −9 to −12‰ VSMOW [20, 21]. This mostly Ca–SO_4-type groundwater was originally meteoric runoff from the Black Forest Highlands that interacted with the SE-dipping Mesozoic sediments (acquiring SO_4 from the evaporites) and laterally infiltrated the Muschelkalk during the Pleistocene (Figure 3(c)) [21].

Deeper within the SMB towards the south (i.e., at the wells of Schafisheim, Pfaffnau, and Berlingen; Figure 1(a)), as well as at the well of Riniken, the salinity of the present-day groundwater increases to 5–11.5 wt.% and NaCl dominates its chemistry [21]. Although the $\delta^{18}O$ signature of this water is not known, the NaCl character and numerous

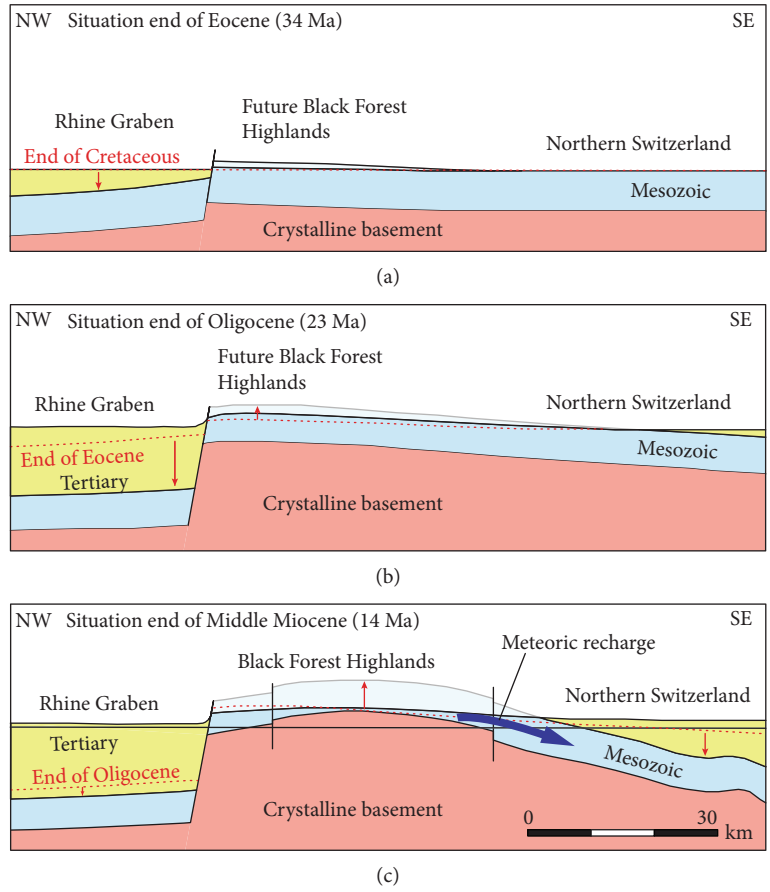

Figure 3: Schematic erosional history along a NW–SE section through the Black Forest Highlands. Middle Miocene exhumation of the Mesozoic (including basal Triassic) sequences and the crystalline basement provided recharge areas for meteoric water (modified after Thury et al. [12]).

other hydrochemical indicators (particularly high $^{40}Ar/^{36}Ar$ and He contents) led Biehler et al. [22] and Waber et al. [21] to suggest that such waters near Baden (i.e., in the area of Riniken; Figure 1(a)) may have ascended into the Muschelkalk along faults from the underlying crystalline basement. Numerous faults that link the basement with the Muschelkalk or that even rise up through the overlying Jurassic and Cretaceous sediments are documented in the region by seismic surveys [15, 23, 24]. For the age of the NaCl groundwaters, isotopic constraints point to at least several million years [21]. Thus, at least at the wells where samples have been taken, the present-day groundwaters in the Muschelkalk are mixtures of dominantly Pleistocene meteoric water and minor amounts of most likely older basement water, with no apparent trace of the original Triassic dolomitizing pore water.

3. Methods

3.1. Petrographic Investigations. Petrography was carried out on thin sections (30 μm thick) via standard transmitted light microscopy and UV-fluorescence microscopy (Olympus U-RFL-T mercury lamp attached to a BX51 microscope).

3.2. Fluid Inclusion Studies. Microthermometry was performed upon gradual heating of doubly polished sections (~100 μm thick) using a Linkam MSD-600 heating-cooling stage mounted on an Olympus BX51 microscope at the Institute of Geological Sciences, University of Bern. The stage was calibrated using phase transitions in CO_2–H_2O and pure H_2O synthetic fluid inclusions, such that measurements below 0°C are accurate to ±0.1°C whereas those between 0 and 100°C are accurate to ±0.5°C.

Laser Raman spectroscopy (Horiba Jobin-Yvon LabRam HR800 confocal instrument) and crushing-stage experiments (method described by Diamond and Marshall [25]) were used to identify gas components within the fluid inclusions.

3.3. Isotope Investigations. Oxygen isotope ratios of pore-filling quartz and kaolinite, as well as hydrogen isotopes of kaolinite, were analysed by conventional bulk techniques at several laboratories: the Scottish Universities Environmental Research Centre (SUERC) in East Kilbride; the Department of Geosciences, University of Lorraine; and the Institute of Earth Surface Dynamics, University of Lausanne (methods described by Sharp [26], Fallick et al. [27], Kasemann et al. [28], Tarantola et al. [29], Jourdan

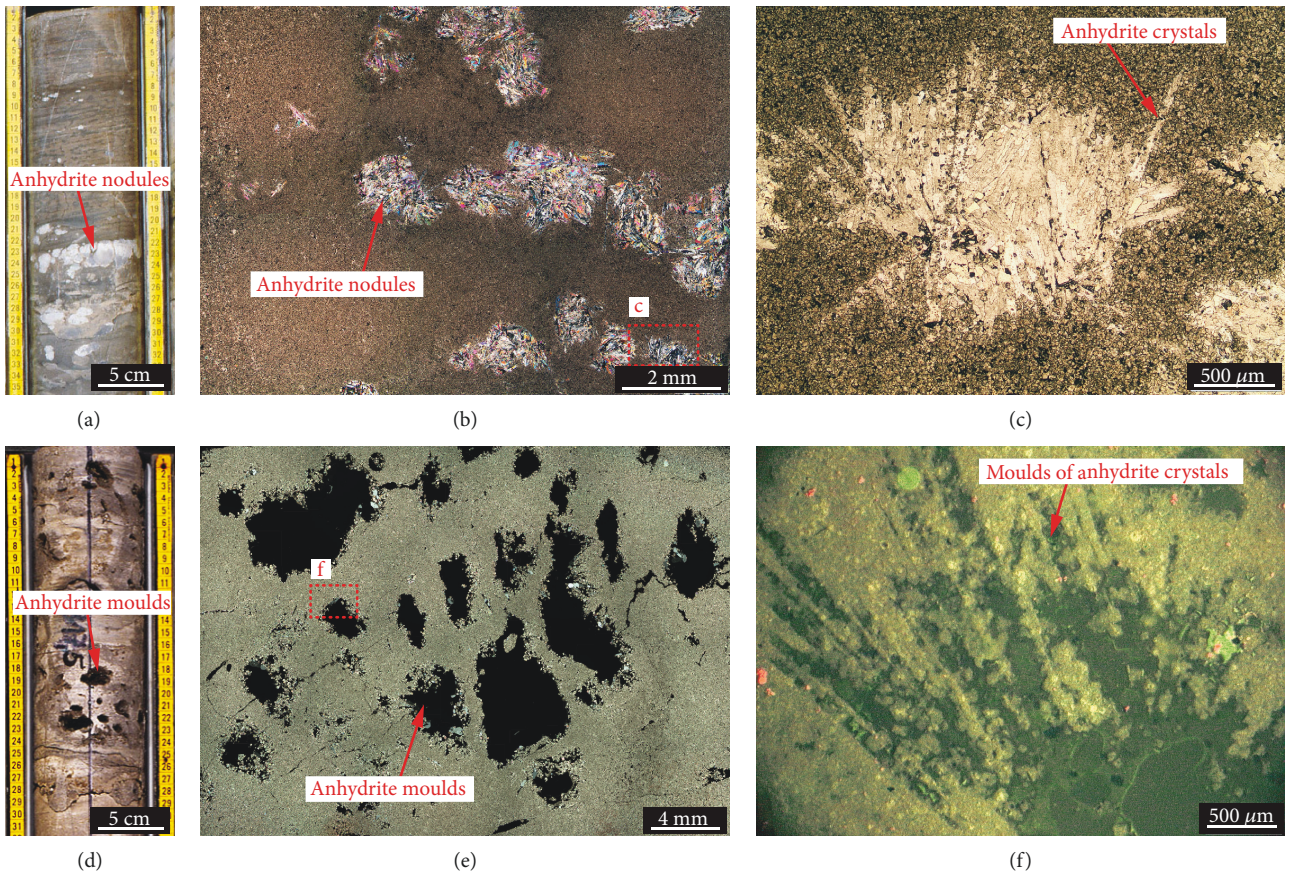

FIGURE 4: Muschelkalk dolostones with (a-c; SLA 1295.80) abundant eogenetic anhydrite nodules or (d-f; BEN 817.59 m) with pores resulting from their dissolution. Photomicrographs in crossed-polarized, transmitted light.

et al. [30]). Oxygen isotope ratios of carbonates, as well as strontium isotope ratios ($^{87}Sr/^{86}Sr$) of carbonates and anhydrite, were measured by conventional bulk techniques at the Institute of Geological Sciences, University of Bern (methods described by Spötl and Vennemann [31] and Krabbenhöft et al. [32]). Sulphur isotope ratios of anhydrite were measured at the Institute of Earth Surface Dynamics, University of Lausanne (method described by Spangenberg et al. [33]). Uranium-lead geochronology of secondary calcites was performed at the Institute of Earth Sciences, University of Toronto, using laser ablation inductively coupled mass spectrometry (LA-ICP-MS; method described by Davis [34, 35]). Numerous spots on polished slabs were first briefly analysed for uranium and common Pb in order to select the most radiogenic targets for dating.

3.4. Fault Distributions and Offsets. The distribution and vertical offsets of faults that crosscut the basement and the overlying Triassic sediments (including the Upper Muschelkalk dolostones) were found by comparing the elevations of neighbouring pixels in the swisstopo-GeoMol digital subsurface model of the Swiss Molasse Basin. The model itself is based on interpretation of seismic surveys, and each of its pixels corresponds to a 100 m x 100 m area.

4. Results

4.1. Evolution of Matrix Porosity. Both the Trigonodus Dolomit and the Dolomit der Anhydritgruppe contain abundant anhydrite nodules (typically a 1–3 cm thick in stratiform aggregates >10 cm long; Figures 4(a)–4(c)) or pores resulting from their dissolution (Figures 4(a)–4(f)). The residual pores consist of mm–dm size, roughly spherical to ellipsoidal cavities that often show characteristic columnar branches radiating from their walls into the rock matrix (Figures 4(e) and 4(f)). The textural match between the shapes of these cavities and the shapes of intact anhydrite nodules (Figures 4(b) and 4(c)) leaves no doubt that the cavities are dissolution moulds.

Core analyses and geophysical log investigations show that the matrix porosity of the Trigonodus Dolomit varies between 8 and 34 vol.% in the shallow wells (mean of 18–23 vol.% at BOZ, SIB, and LEU; Figure 1(a)) and between 0 and 12 vol.% in the deep wells (mean of 3–8 vol.% at LIN, BER, KRE, and HER; Figure 1(a)) [36]. The dissolution of anhydrite nodules was found to have increased bulk porosity by up to 15 vol. %.

This type of porosity is heterogeneously distributed across the SMB. At the shallow wells along the northeastern margin of the basin, the anhydrite nodules are completely

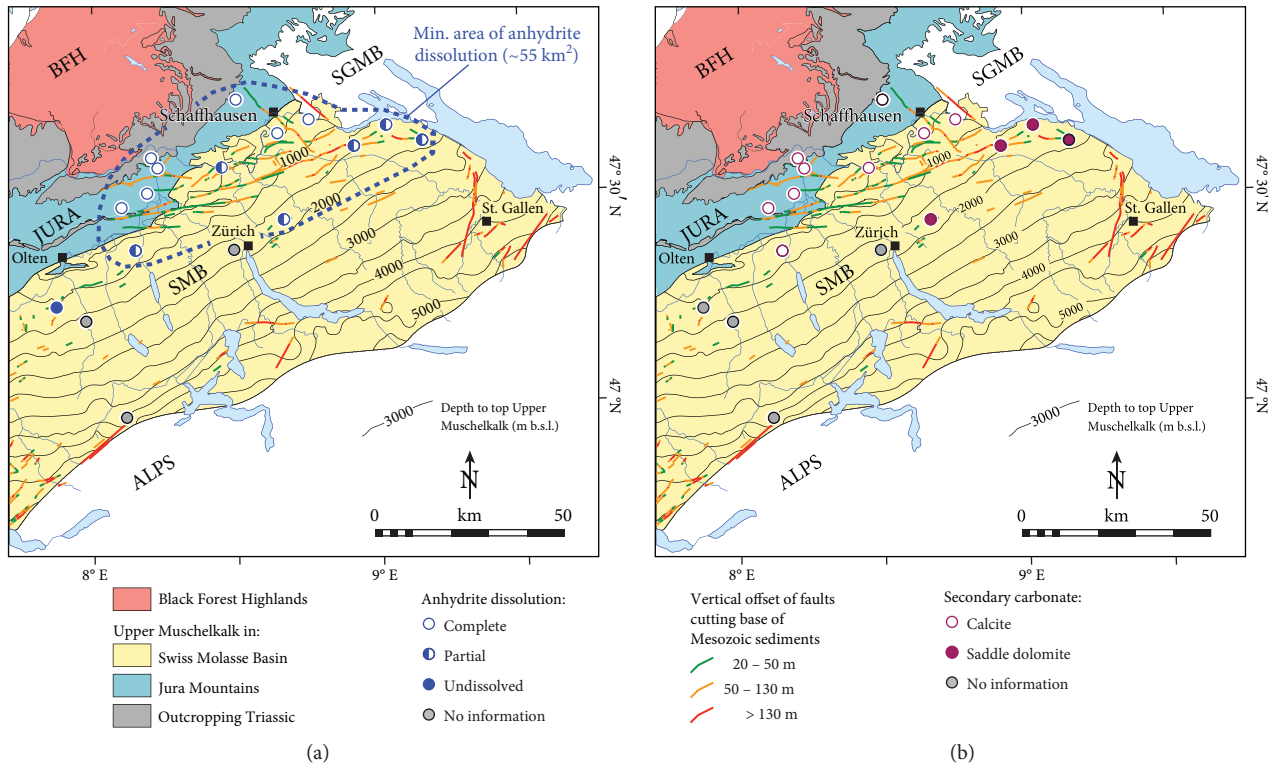

FIGURE 5: (a) Spatial distribution of anhydrite-dissolution pores within the Trigonodus Dolomit of the NE Swiss Molasse Basin (SMB). Depth contours are in m below sea level (BFH: Black Forest Highlands; SGMB: South German Molasse Basin; modified after Müller et al. [15] and Sommaruga et al. [24]). Faults emanating from the basement into the Upper Muschelkalk have been deduced from the GeoMol digital subsurface model (this study). See Figure 1(a) and Table A.1 for well names. (b) Spatial distribution of secondary calcite and saddle dolomite filling pores and fractures.

dissolved, whereas at the deeper, southern wells the anhydrite is only partially dissolved or it remains entirely unaffected by dissolution (Figure 5(a)).

In the shallow wells (Bözberg, Böttstein, and Siblingen) where no pressure solution between dolomite crystals has occurred, the matrix dolomite retains smooth crystal faces and sharp edges, attesting to its chemical equilibrium with the pore waters, irrespective of whether anhydrite is dissolved or not. Where the anhydrite is dissolved, the resulting pore space is often partly filled by secondary minerals (Figure 5(b)).

Anhydrite moulds are not the only macroscopic pores in the studied dolostones. Vertical to subvertical fractures with apertures up to 0.5 cm occasionally traverse the rocks, and they are locally filled or partly filled with secondary minerals. The various events of secondary mineral precipitation within the dissolution cavities and fractures are described in the following and summarized in Figure 6.

(1) The first precipitation event formed assemblages of quartz, pyrite, minor sphalerite, and rarely galena within pores and fractures. The abundance of these minerals is generally very low, resulting in only minimal pore clogging. In the anhydrite moulds, the individual quartz crystals contain tiny solid inclusions of relict anhydrite. The inclusions are widely spaced relative to their sizes and are thus supported by the quartz matrix, indicating that the quartz precipitated during anhydrite dissolution (Figures 7(a) and 7(b)).

(2) A second, younger event of pore clogging is quantitatively more important and involved precipitation of assemblages of calcite, kaolinite, and minor barite and fluorite, leading locally to complete clogging of the available pore space. Calcite–kaolinite intergrowths indicate that the two minerals precipitated at least in part simultaneously and they both occur in within anhydrite moulds, as well as fracture fillings (Figures 7(c)–7(f)).

(3) A third event involved precipitation of secondary anhydrite, often as a replacement of calcite within the moulds and the fractures, indicating that it postdates calcite and its associated minerals (Figure 7(g)).

(4) Another event involved precipitation of saddle dolomite, also leading to significant clogging of fractures and of anhydrite moulds. Whereas overgrowth textures show that saddle dolomite postdates quartz and its associated minerals (Figure 7(h)), the relative timing of dolomite with respect to calcite precipitation is unclear, as they are spatially separated:

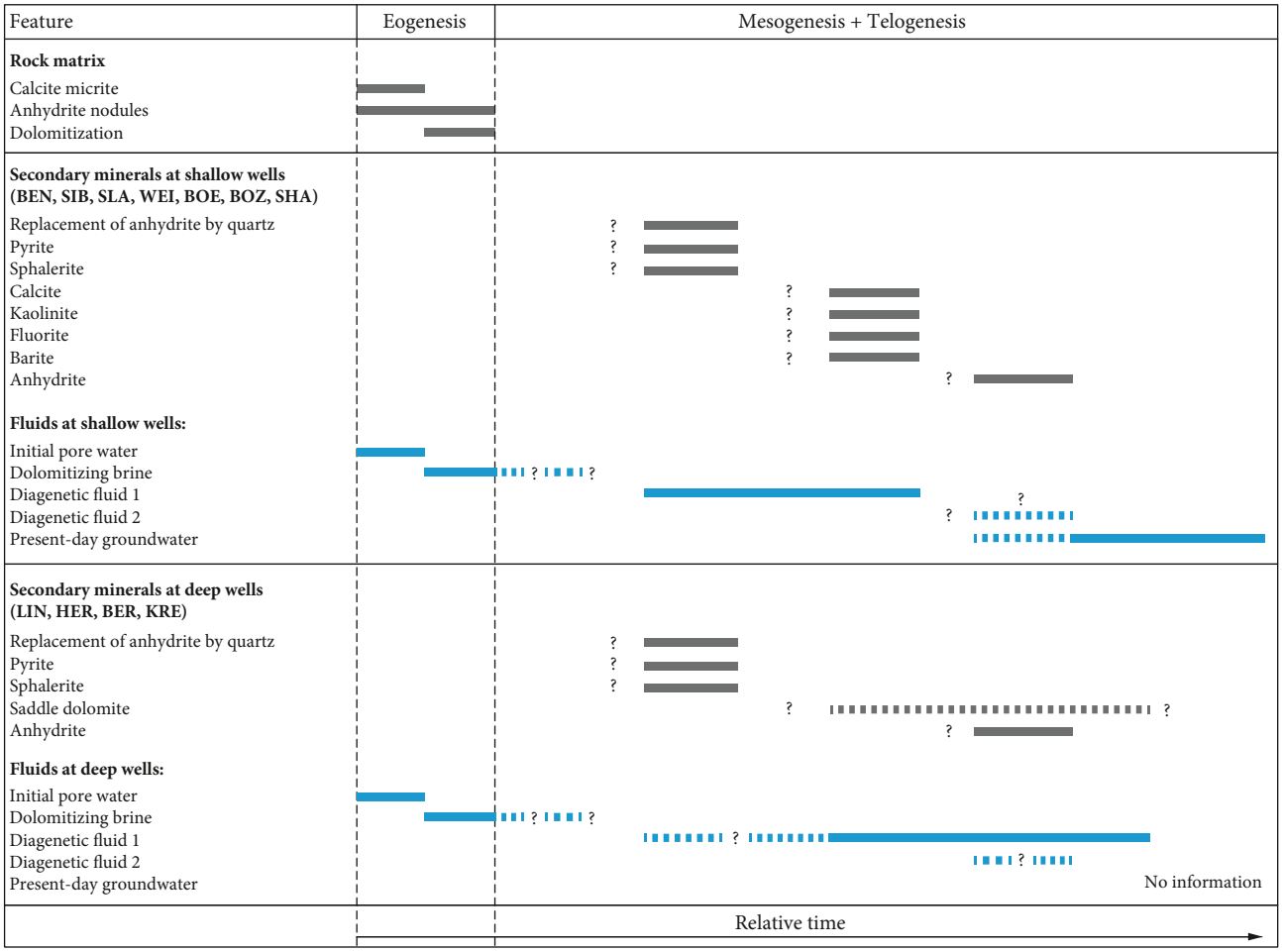

Figure 6: Paragenetic sequences of secondary minerals in dissolution cavities and fractures in the shallow wells along the northern margin of the Swiss Molasse Basin compared to those in the southern, deeper wells.

secondary calcite and associated minerals are restricted to the shallow northern margin of the SMB, whereas saddle dolomite occurs in the southern, deeper wells (Figure 5(b)).

4.2. Strontium Isotope Ratios. Figure 8 (data in Table A.2) shows the strontium isotope ratios of the rock matrix, anhydrite nodules, and secondary pore- and fracture-filling minerals in the Muschelkalk carbonates. In order to trace and identify potential mineral parent-waters, strontium isotope ratios of primary anhydrite and secondary calcite pore and fracture fillings from underlying and overlying units, as well as of the recent groundwater, were collated from the literature and compared in the same diagram. Calcite pore and fracture fillings in the Muschelkalk both display a wide range of strontium isotope ratios (0.70798–0.71629), which partly overlaps the Sr signatures of the rock matrix and the early diagenetic anhydrite nodules. However, a large portion of the calcites show distinctly higher values. Saddle dolomite also shows high $^{87}Sr/^{86}Sr$ ratios, although the scatter in its data is distinctly smaller than that of the calcite.

Importantly for tracing the fluids that transported the above secondary minerals, several rocks and groundwaters within the local stratigraphy are characterized by high $^{87}Sr/^{86}Sr$ ratios: the rock matrix of the underlying Variscan gneiss basement and the Buntsandstein (values of 0.714–0.728, partly off-axis in Figure 8), the pore- and fracture-filling calcite in the latter two units, the present-day groundwaters in these units, and the shallow groundwater and meteoric river runoff from the crystalline rocks exposed in the Black Forest Highlands.

4.3. Fluid Inclusion Studies. Our fluid inclusion studies have focussed on secondary pore and fracture fillings in the Muschelkalk carbonates and fracture fillings in the underlying crystalline basement. Many of the host minerals contain fluid inclusions arrayed along healed fractures that intersect or crosscut crystal boundaries. These inclusions were not studied in detail because they evidently postdate the precipitation of the host mineral. All the fluid inclusions analysed in this study are either arrayed along former growth horizons of their host crystals, or they occur as dense, three-dimensional clouds within the cores of their host crystals, mantled by inclusion-free crystal rims (Figures 9(a)–9(c)). Thus, they are by definition primary inclusions. It follows that they were trapped during growth of their host crystals and hence the

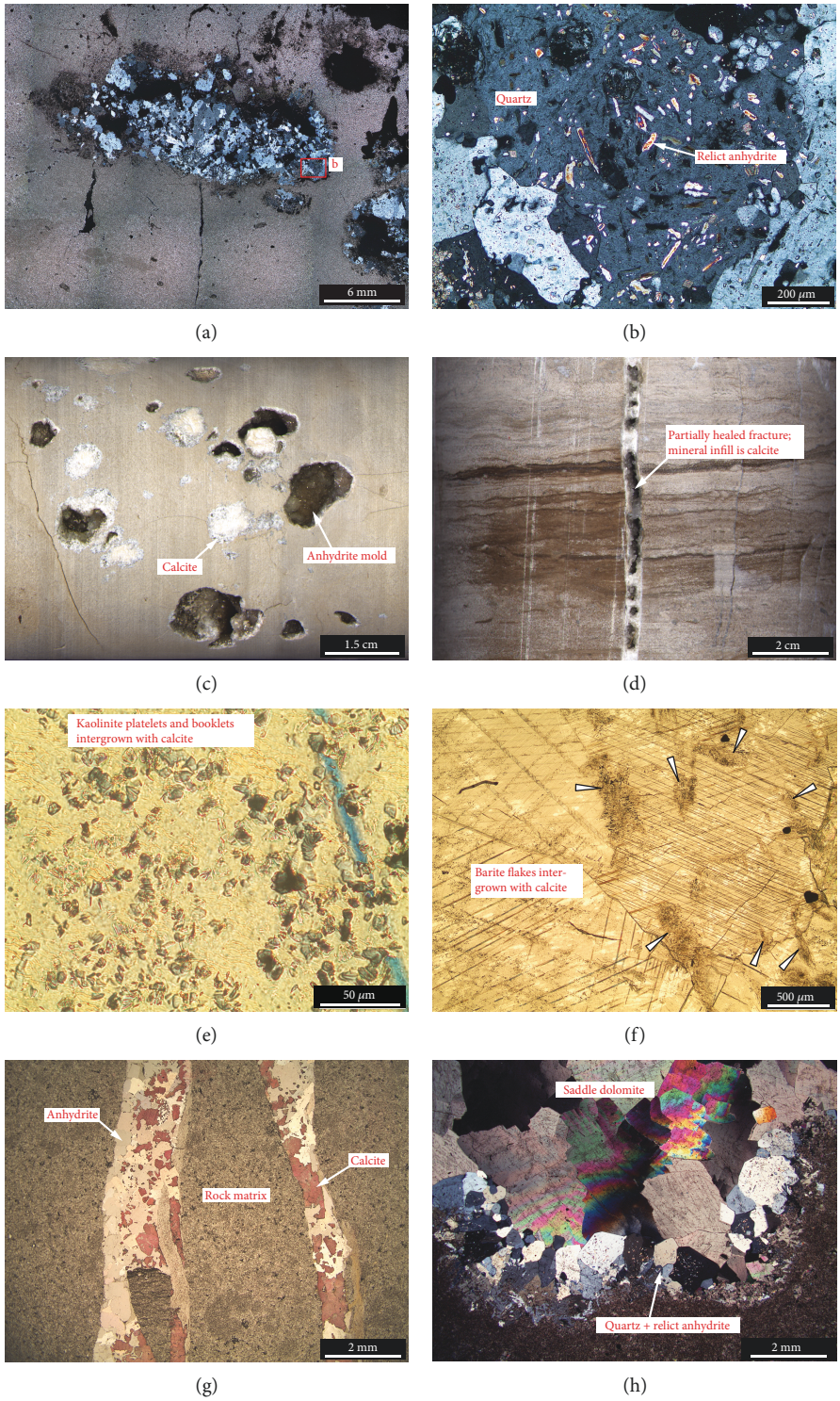

Figure 7: (a) Secondary quartz filling an anhydrite mould in the Trigonodus Dolomit (BEN 825.11 m). (b) The quartz contains tiny, distributed inclusions of pyrite and relict anhydrite, indicating that the quartz precipitated during anhydrite dissolution and thus is associated with the formation of the anhydrite-dissolution pores (BEN 825.11 m). (c) Second-stage calcite clogging anhydrite moulds in the Muschelkalk (BOZ 81.90 m). (d) Calcite in fractures (SLA 1170.83 m). (e) Intergrowths of kaolinite and calcite filling an anhydrite mould (SLA 1135.29 m). (f) Intergrowths of barite (arrowheads) and calcite filling an anhydrite mould (SLA 1164.33 m). (g) Anhydrite occasionally replaces calcite within moulds and fractures in the Muschelkalk (calcite stained with Alizarin Red; SLA 1123.83 m). (h) Saddle dolomite filling anhydrite moulds in the deeply buried Muschelkalk. Saddle dolomite postdates secondary quartz and associated minerals (BER 2189.11 m) (a, b, h: crossed-polarized, transmitted-light microscopy; e–g: plane polarized, transmitted-light microscopy; c, d: reflected-light photograph of drill core).

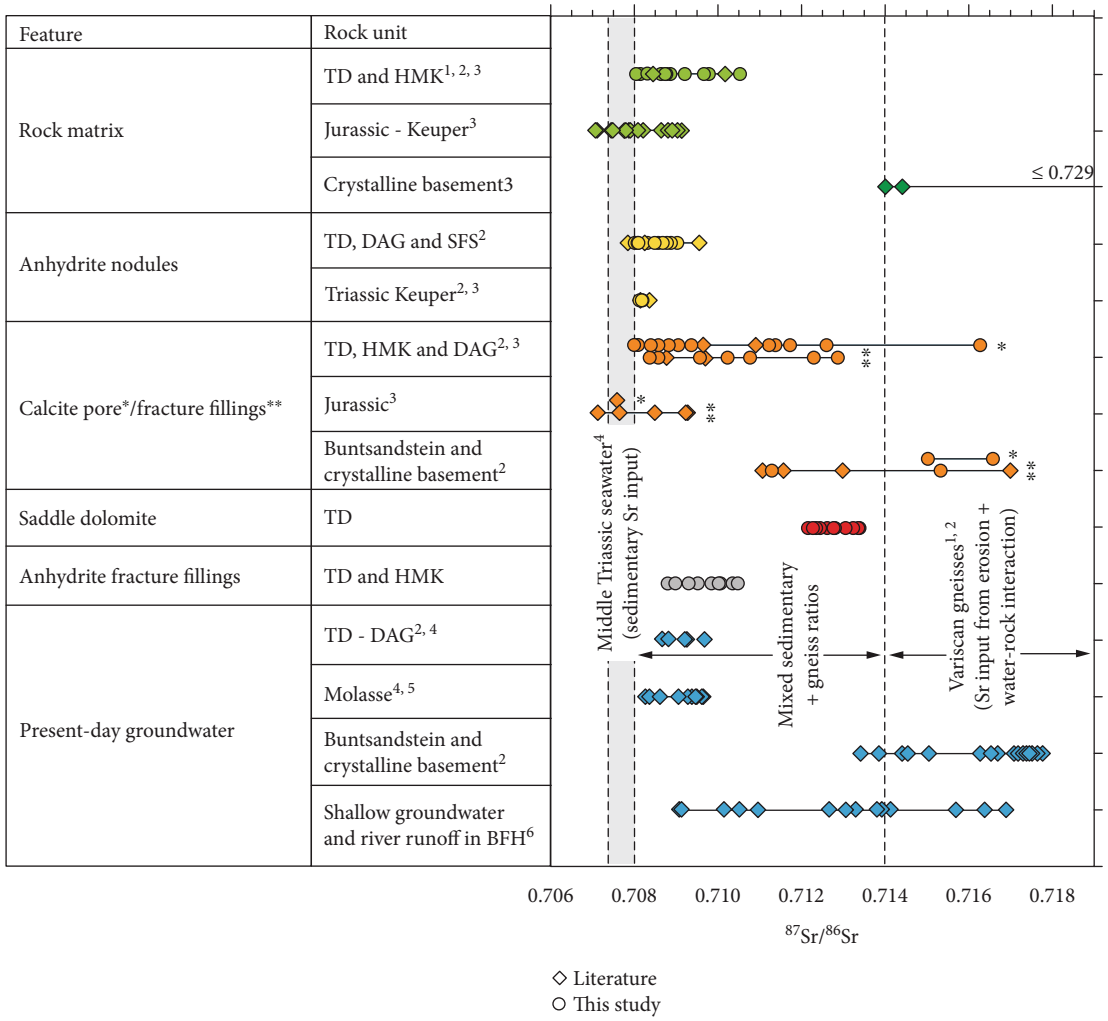

Figure 8: Strontium isotope ratios of minerals, rocks, and recent groundwater in the Upper Muschelkalk and in overlying and underlying units (TD: Trigonodus Dolomit; HMK: Hauptmuschelkalk; DAG: Dolomit der Anhydritgruppe; SFS: Sulfatschichten; BFH: Black Forest Highlands; [1][37], [2][20], [3][38], [4][39], [5][21], [6][40]).

data obtained from the analyses are representative of the free parent-fluids at the time of mineral precipitation.

At room temperature, all the primary inclusions in quartz and calcite contain a bubble of methane surrounded by aqueous liquid, although the volumetric ratios of the two phases vary strongly between inclusions within the same coeval group (i.e., within the same fluid inclusion "assemblage"; Figures 9(d) and 9(e)). This variation is interpreted to mean that both fluid phases were present at mutual saturation during entrapment of the inclusions [41]; i.e., entrapment was heterogeneous. Methane in the inclusions was unequivocally identified by crushing-stage experiments on samples immersed in naphtha, but it proved to be undetectable by laser Raman spectroscopy, indicating that its pressure within the inclusions is low. Primary fluid inclusions in saddle dolomite display uniform volume fractions of liquid and vapour within individual assemblages, demonstrating that they were trapped from a single-phase aqueous liquid (i.e., homogeneously; Figure 9(f)).

In primary fluid inclusions in quartz and calcite, only two types of equilibrium phase transitions could be measured in the inclusions by microthermometry: (1) the final melting of ice in the presence of liquid and vapour, $T_m(\text{ice})$ and (2) homogenization, either via a bubble-point transition to the liquid state, $T_h(\text{LV} \rightarrow \text{L})$, or via a dew-point transition to the vapour state $T_h(\text{LV} \rightarrow \text{V})$. In each inclusion, the phase transitions are reproducible upon repeated heating and cooling cycles, although the dew-point measurements are typically underestimates of the true values, owing to difficulties in observing the final disappearance of the liquid wetting the inclusion walls. Fluid inclusion trapping temperatures, T_{trap}, were therefore taken as being equal to the lowest $T_h(\text{LV} \rightarrow \text{L})$ value measured in each assemblage, following the approach by Diamond [41, 42]. Due to the small sizes of the inclusions (i.e., in the range of 10 μm), no reliable eutectic temperatures could be determined. No methane clathrate was observed, consistent with the low internal pressure of the inclusions below the ice +

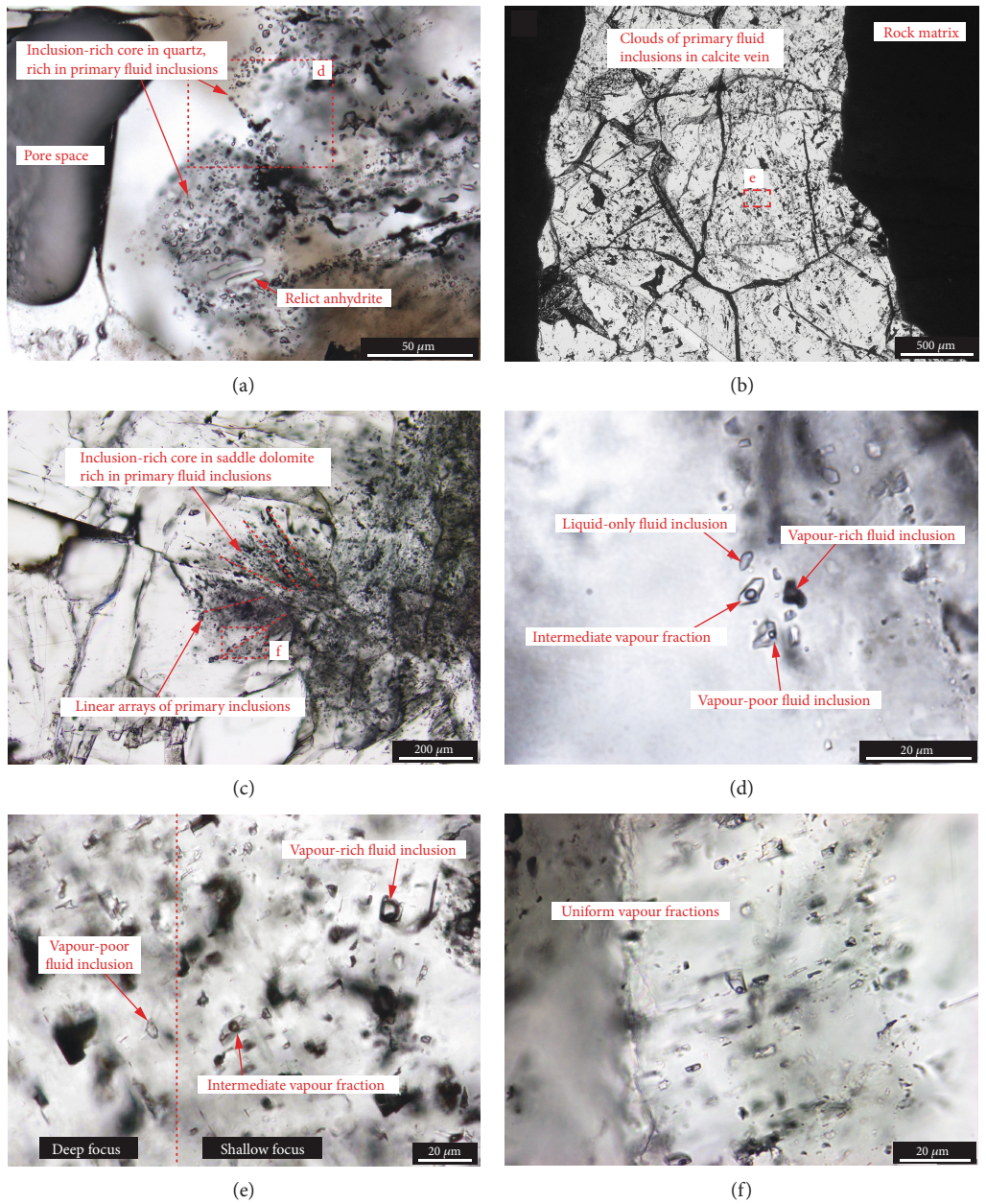

FIGURE 9: Assemblages of primary fluid inclusions in secondary minerals. (a) Quartz (SLA 1127.44 m). (b) Calcite (SIB 241.60 m). (c) Saddle dolomite (LIN 2245.35 m). Variations in phase proportions show that primary inclusions in (d) quartz and (e) calcite were heterogeneously trapped, whereas primary fluid inclusions in (f) saddle dolomite were homogeneously trapped (see text for details; plane polarized, transmitted-light microscopy).

water + CH_4-clathrate + vapour Q_1 equilibrium at 26 bar [42]. The results of the microthermometric analyses are shown in Figure 10 and Table A.3.

In the Muschelkalk, the trapping temperatures of pore-filling quartz from the wells at Benken and Schlattingen vary within the range of 41–58°C. In contrast, the paragenetically younger pore- and fracture-filling calcites were trapped at distinctly higher temperatures of 76–89°C. These latter temperatures are slightly higher than those modelled for Miocene maximum burial at these wells but lower than the temperatures modelled for Cretaceous maximum burial (Figure 2). Primary fluid inclusions in secondary calcites from the wells at Siblingen, Böttstein, Schafisheim, and Bözberg yield trapping temperatures of 51–85°C. However, for these wells no temperature constraints from basin modelling are available for comparison.

The homogeneous trapping mode of primary fluid inclusions in saddle dolomite from the wells at Lindau and Berlingen implies that their T_h values between 138 and 147°C constitute minimum trapping temperatures [41]. Assuming fluid entrapment at maximum burial depth (~2700 m; [9]) under hydrostatic conditions (i.e., ~26.5 MPa), the isochores of these low-salinity inclusions (see below for salinities) yield corrected trapping temperatures between

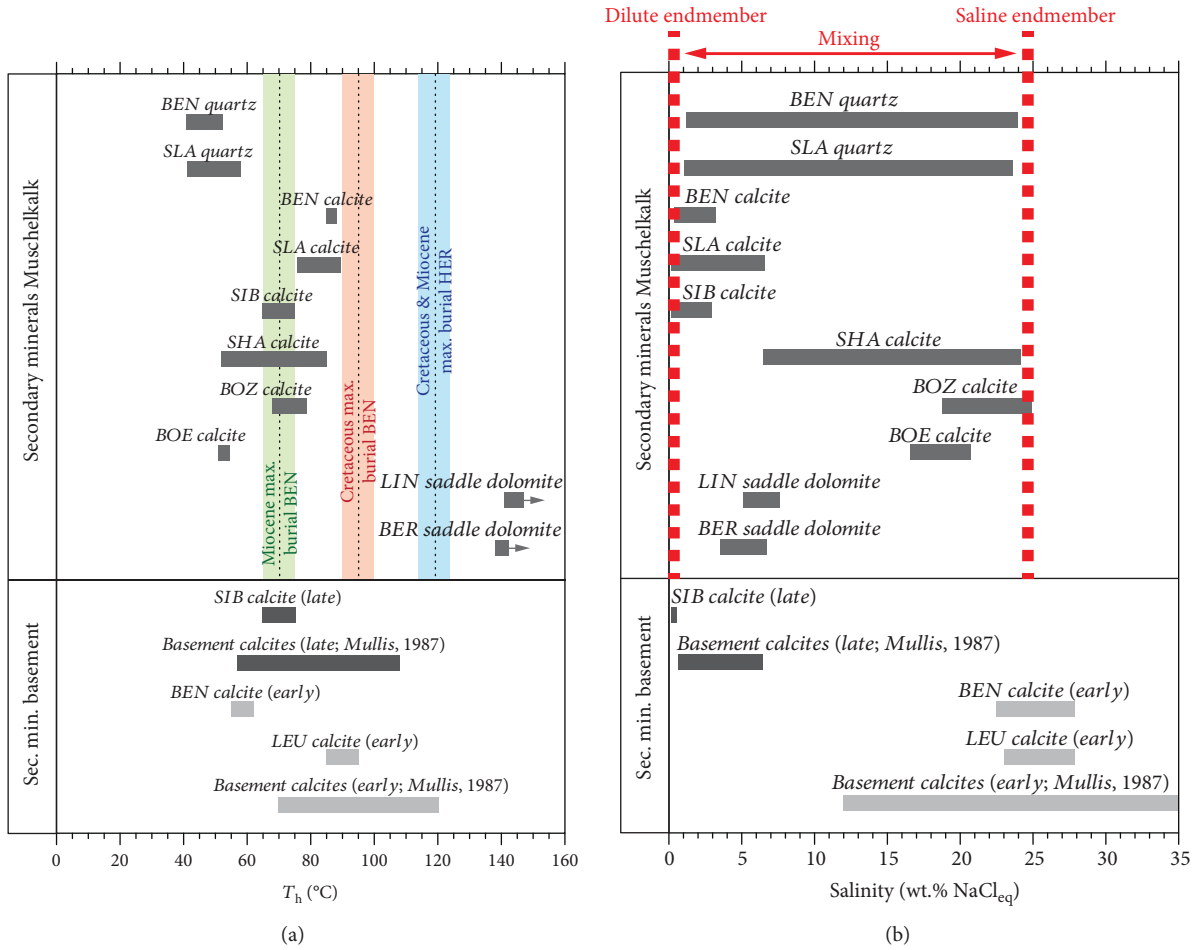

FIGURE 10: Microthermometric results from primary fluid inclusions in secondary minerals from the Muschelkalk and the crystalline basement at various wells across the Swiss Molasse Basin. (a) Homogenization temperatures (T_h). For the data from Mullis [43] and for saddle dolomites, the T_h values correspond to minimum temperatures of fluid trapping. For all other data, T_h corresponds to the exact trapping temperature (see text for explanation). Maximum rock temperatures during Cretaceous and Miocene maximum burial (Figure 2) are plotted for comparison. (b) Salinities calculated from ice-melting temperatures.

152 and 161°C. These temperatures are distinctly higher than the maximum burial temperatures of ~115°C derived from basin modelling at the nearby well of Herdern (Figure 2).

Salinities in terms of equivalent NaCl concentrations were calculated from the T_m(ice) values using the calibration of Hall et al. [44] and are illustrated in Figure 10(b). In the Muschelkalk pore-filling quartz, primary inclusions from the Benken and Schlattingen wells show highly variable salinities of 1.2–23.9 wt.% $NaCl_{eq}$ (salinity variations within individual fluid inclusion assemblages are up to 17 wt.% $NaCl_{eq}$). In contrast, paragenetically younger pore- and fracture-filling calcites from these wells contain primary inclusions with relatively uniform and distinctly lower salinities in the order of 0.2–6.5 wt.%. Similarly low salinities of calcite parent-water are observed at the well of Siblingen (0.2–2.9 wt.% $NaCl_{eq}$). In contrast, primary fluid inclusions in secondary calcite from the wells at Böttstein, Bözberg, and Schafisheim show higher and variable salinities ranging from 6.5 to 24.9 wt.% $NaCl_{eq.}$ (at the Schafisheim well, salinity variations within individual inclusion assemblages are up to 16 wt.% $NaCl_{eq}$). Primary fluid inclusions in saddle dolomite from the wells at Lindau and Berlingen show salinities within a relatively narrow range of 3.6–7.6 wt.% $NaCl_{eq}$.

In fracture-filling calcite from the crystalline basement, two generations of primary fluid inclusions were identified. One has low salinity (Siblingen: 0.2–0.5 wt.% $NaCl_{eq.}$) and trapping temperatures of 65–75°C, whereas the other shows high salinities (Leuggern, Benken: 22.5–27.8 wt.% $NaCl_{eq}$) and trapping temperatures of 55–95°C. The two generations occur in spatially separated host crystals and thus their relative timing cannot be determined. However, Mullis [43] investigated predominantly secondary inclusions in secondary calcites from the crystalline basement and the Buntsandstein and found a transition from early high-salinity inclusions (12 to >23.3 wt.% $NaCl_{eq.}$ and T_h of 70–149°C) to late, low- to intermediate-salinity inclusions (1.2–6.4 wt.% $NaCl_{eq.}$ and T_h of 57–108°C; data reported in Matter et al. [45] and Peters et al. [46, 47]). These salinity values are in good agreement with the data obtained in this study (Figure 10). Accordingly, it is assumed that the relative timing of the fluid generations in the basement calcites

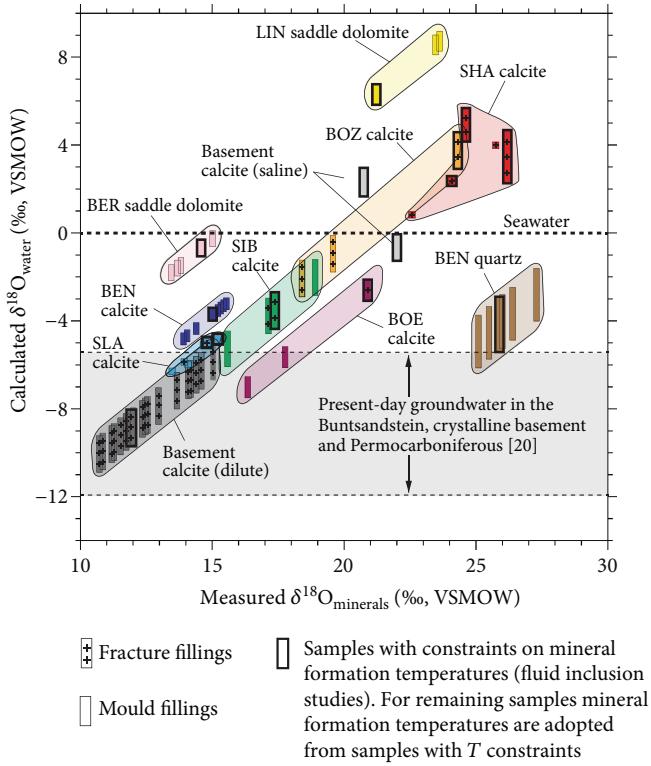

Figure 11: Measured and calculated oxygen isotopic compositions of parent-waters of secondary carbonates and quartz, as well as literature data for the recent groundwater in the crystalline basement (grey area; [20]). The ranges of calculated $\delta^{18}O$ of the parent waters result from the ranges of fluid inclusion trapping temperatures shown in Figure 10 and Table A.3.

investigated in this study is the same as that deduced by Mullis [43], i.e., early high-salinity and later low-salinity fluid generations.

4.4. Oxygen Isotopes of Calcite, Saddle Dolomite, and Quartz. Figure 11 (data in Table A.4) shows the oxygen isotope analyses of secondary calcite, saddle dolomite, and quartz (Figure 11), as well as the isotopic signatures of their corresponding parent-waters (Figure 11) calculated from average fluid inclusion trapping temperatures and the isotope fractionation factors given by Friedman & O'Neil [48] and Zheng [49]. Analyses of carbon isotopes in the secondary carbonates revealed no sensitivity to the mixing processes described in Section 5 and so the data are not presented herein.

In the Muschelkalk, the calculated parent-water of the saddle dolomite at the well of Lindau shows the highest $\delta^{18}O$ signatures, between 6.1 and 9.0‰ VSMOW. Calcite parent-waters at the well of Schafisheim show lower $\delta^{18}O$ signatures of 0.9 to 5.6‰ VSMOW, whereas at the well of Bözberg, values of −2.8 to 4.4‰ VSMOW are obtained. Saddle dolomite at the well of Berlingen shows similar oxygen isotopic signatures. Calcite parent-waters at the wells of Benken, Schlattingen, Böttstein, and Siblingen show the lowest $\delta^{18}O$ values (−7.4 to −1.3‰ VSMOW), which fall within the same range as the parent-water of the secondary quartz at the well of Benken (−6.1 to −1.7‰ VSMOW).

In the crystalline basement, the two generations of secondary calcite identified by their differing primary fluid inclusions (Section 4.4; Figure 10) can be further distinguished by their different $\delta^{18}O$ and Sr-isotopic signatures. The early-generation, high-salinity calcite from the Benken and Leuggern wells shows $\delta^{18}O$ values of 20.8 to 22.0‰ VSMOW, corresponding to parent waters of −0.7 to 2.3‰ VSMOW (Figure 11). The $^{87}Sr/^{86}Sr$ ratio of the calcites is 0.7112. In contrast, the late-generation, low-salinity calcite from the Siblingen well shows a $\delta^{18}O$ value of 11.9‰ VSMOW, which corresponds to a parent water of −8.9‰ VSMOW (Figure 11). The $^{87}Sr/^{86}Sr$ ratio of this calcite is 0.7154. The trapping temperatures of primary fluid inclusions in secondary low-salinity calcite at the well of Siblingen (65–75°C; Figure 10) have further been used to calculate the parent-water of secondary calcites from other boreholes at similar depths (1023 ± 300 m), for which no fluid inclusion data are available but which show similarly light $\delta^{18}O$ signatures (Figure 11; [46, 47, 50, 51]). The calculations show that the parent-waters had $\delta^{18}O$ values ranging from −10.7 to −5.0‰ VSMOW. These values largely overlap with the present-day groundwater in the Buntsandstein and the crystalline basement [20].

4.5. Oxygen and Hydrogen Isotopes of Kaolinite. Figure 12 (data in Table A.5) shows the calculated $\delta^{18}O$ and $\delta^{2}H$ signatures of the kaolinite parent-waters in the Muschelkalk at the wells of Benken and Schlattingen. Petrographic investigations have shown that the secondary calcite at least partially coprecipitated with kaolinite (Figures 7(c) and 7(d)). Accordingly, $\delta^{18}O$ and $\delta^{2}H$ signatures of the

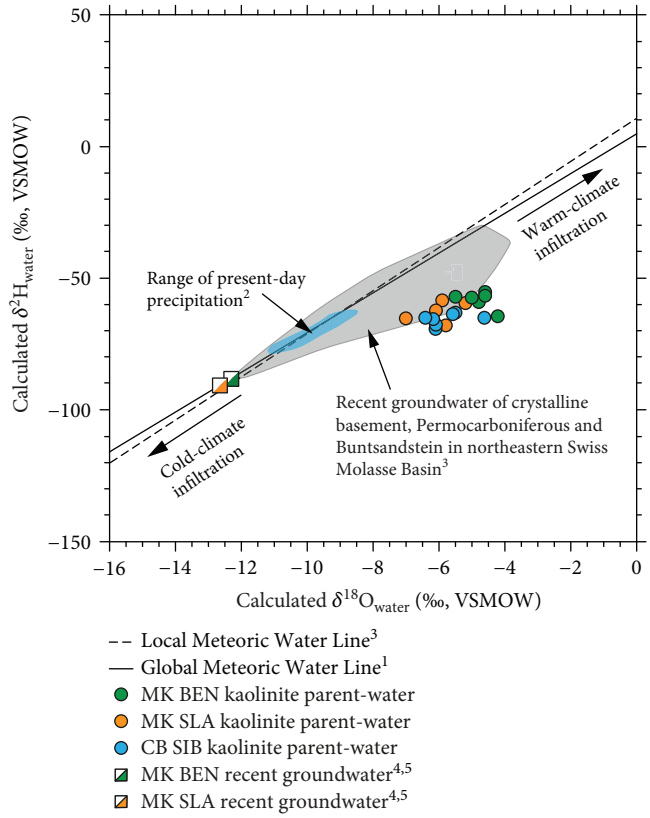

Figure 12: Calculated oxygen and hydrogen isotopic composition of the parent water that precipitated kaolinite and cogenetic calcite in the Muschelkalk (MK) and in the crystalline basement (CB) at the wells of Benken (BEN), Schlattingen (SLA), and Siblingen (SIB). Shown for comparison are the Local and Global Meteoric Water Lines, present-day precipitation, recent groundwater in the Muschelkalk and in the underlying crystalline basement, and Permocarboniferous and Buntsandstein within the NE-Swiss Molasse Basin. [1][54], [2][55], [3][20], [4][38], [5]this study.

kaolinite parent-waters were calculated based on the measured isotopic composition of the kaolinite (Table A.5), the fluid inclusion trapping temperatures of secondary calcite (Table A.3), and the isotope fractionation factors given by Sheppard and Gilg [52]. Regarding the fracture-filling kaolinite in the crystalline basement, Mazurek [53] noted that the wall rocks are often affected by kaolinite alteration and that some of the fractures contain calcite in addition to kaolinite. The fluid inclusion data in Figure 10 (SIB basement calcite; low-salinity) are from calcite in a kaolinite-free fracture, but kaolinite is present in the adjacent altered wall rock. We therefore assume that the 65–75°C trapping temperatures of the primary inclusions in calcite also apply to the precipitation of kaolinite and so the parent-water of the kaolinite was calculated from this temperature.

The parent-water of the Muschelkalk kaolinite shows oxygen and hydrogen isotopic compositions of −7.6 to −3.4‰ VSMOW and −66.5 to −55.1‰ VSMOW, respectively. These values fall to the right of the local meteoric water line, and they deviate significantly from the recent groundwater in the Muschelkalk dolostones. In contrast, they overlap with the oxygen and hydrogen isotopic compositions of the recent groundwater in the underlying Buntsandstein and in the Variscan gneiss basement (grey field in Figure 12). Furthermore, the calculated parent-water of kaolinite in the Muschelkalk (green and orange dots in Figure 12) shows very similar oxygen and hydrogen isotopic signatures to the parent-water of kaolinite in the crystalline basement (blue dots in Figure 12).

4.6. Sulphur Isotopes of Anhydrite. Figure 13 (data in Table A.6) illustrates the sulphur isotopic composition of primary anhydrite and secondary anhydrite fracture fillings from the Muschelkalk and the overlying Keuper. Primary anhydrite from those sedimentological groups shows distinctly different $\delta^{34}S$ values from 18.0 to 19.9‰ VCDT in the Muschelkalk and from 12.5 to 15.9‰ VCDT in the Keuper. These values are in perfect agreement with the studies performed by Pearson et al. [20], who found $\delta^{34}S$ values of 17–21‰ VCDT in primary anhydrite of the Muschelkalk and 10–17‰ VCDT in equivalents from the Keuper. In both the Keuper and the Muschelkalk, the $\delta^{34}S$ values of secondary anhydrite fracture fillings fall within the ranges of the primary anhydrite in their wall rocks (Figure 13).

4.7. U-Pb Geochronology of Calcites. The results of the LA-ICP-MS analyses of secondary calcites from the wells at Benken, Schlattingen, Siblingen, and Leuggern are illustrated on Wetherill concordia diagrams ($^{206}Pb/^{238}U$ vs. $^{207}Pb/^{235}U$) in Figures 14(a)–14(h) (data in Table A.7). The error ellipses

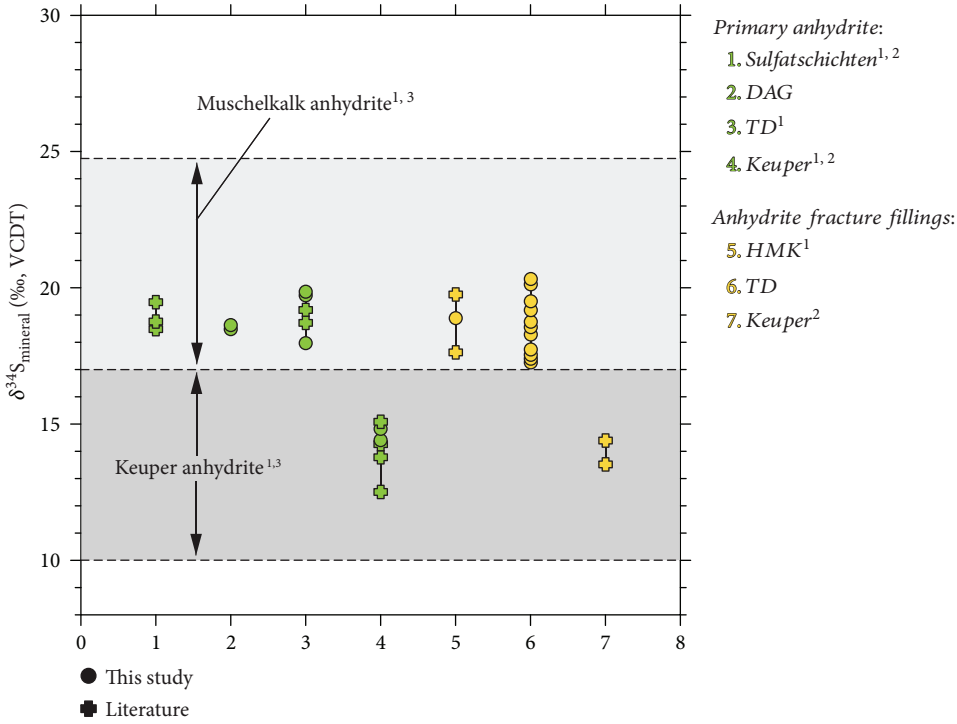

Figure 13: Sulphur isotopic composition of primary anhydrite in the Sulfatschichten (Middle Muschelkalk), the Dolomit der Anhydritgruppe (DAG), the Trigonodus Dolomit (TD), and the Keuper compared to those of secondary anhydrite fracture-fillings in the Hauptmuschelkalk (HMK), TD, and Keuper. [1][20], [2][38], [3][56].

in the diagrams are reported at two sigma. Note that because ^{204}Pb cannot be measured accurately, a correction for common lead is not feasible. Therefore, measurements of total instead of radiogenic Pb are plotted. The presence of common Pb has the effect of shifting the data to the right and upward towards an age of approximately 5000 Ma. Hence, multiple data with a similar age but different levels of common Pb will form a linear array on the concordia plot with the lower concordia intercept giving the age of the radiogenic component [34]. Thus, the age can be obtained independently of assumptions about the isotopic composition of the common Pb component by projecting the regression line of data points towards concordia.

A total of 26 samples were analysed; however, only 8 provided meaningful ages. The remaining samples contained either insufficient uranium or too much common lead. All the datable calcite samples show a substantial radiogenic component, as illustrated by the near-concordant ages, and the isotope ratios generally show a small scatter. Accordingly, they align well with the corresponding radiogenic–common Pb mixing lines, thus yielding single ages. Six secondary calcites from the Muschelkalk provided mean ages between 11.5 and 16.8 Ma (Figures 14(a)–14(f)). Two secondary calcites from the crystalline basement yielded mean ages of 8.3 and 13.3 Ma (Figures 14(g) and 14(h)).

5. Discussion

5.1. Secondary Minerals in Dissolution Moulds versus Fractures. The anhydrite-dissolution moulds and the subvertical fractures in the Muschelkalk dolostones contain almost the same sequences of secondary minerals. Both contain early quartz + pyrite and a later paragenesis of calcite + kaolinite ± fluorite ± barite. The strontium isotope ratios of the calcite in the moulds matches those of calcite in the fracture fillings (Figure 8), and at the wells of Schlattingen and Siblingen, the parent waters of calcite in both settings show similar oxygen isotope signatures (Figure 11). Furthermore, calcite in the two settings has the same U/Pb age (Figures 14(a)–14(f)). It follows that both pore types (i.e., dissolution cavities and subvertical fractures) were open to influx of the same sequence of parent solutions that deposited the secondary minerals. Therefore, no distinction need be made between the two pore types in the remainder of this discussion.

5.2. Fluid Mixing as the Trigger for Anhydrite Dissolution. As outlined in Section 2.3, upon commencement of burial, the Muschelkalk dolostones contained a highly saline pore water (with δ^{18}O likely between 3 and 8‰ VSMOW) that was in chemical equilibrium with anhydrite and dolomite. Later dissolution of the anhydrite must have been caused by influx of another solution, such that the new pore water was undersaturated with respect to anhydrite but saturated with respect to dolomite (dolomite crystal faces have remained smooth, without dissolution features, up to today). The nature of the fluid that dissolved the anhydrite is revealed by the primary fluid inclusions in quartz, which precipitated during dissolution of anhydrite (Section 4.1). Within groups of coeval fluid inclusions, salinities vary widely between 1 and 24 wt.% $NaCl_{eq}$ (Figure 10(b)). These observations imply that mixing of two waters with contrasting salinities induced the

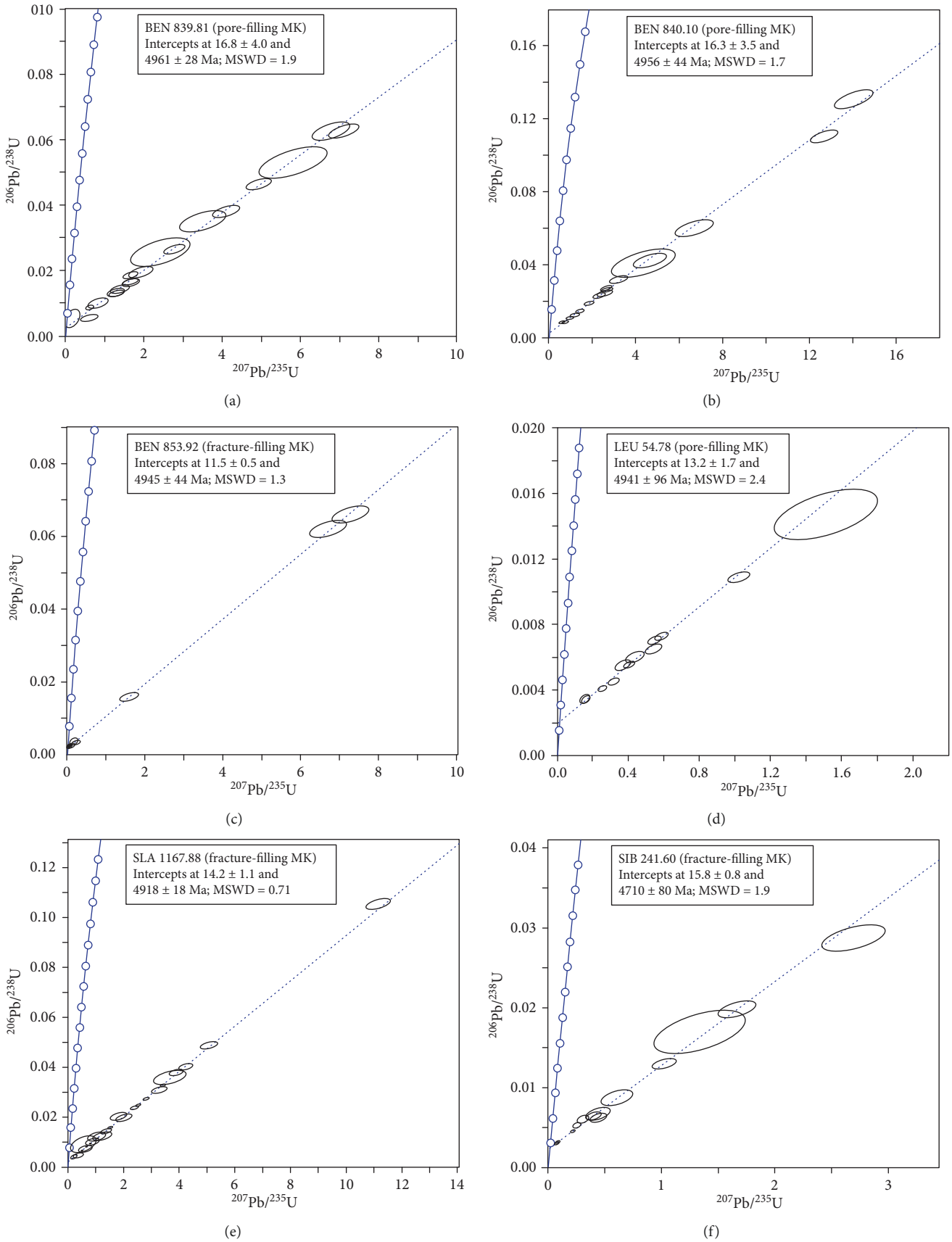

Figure 14: Continued.

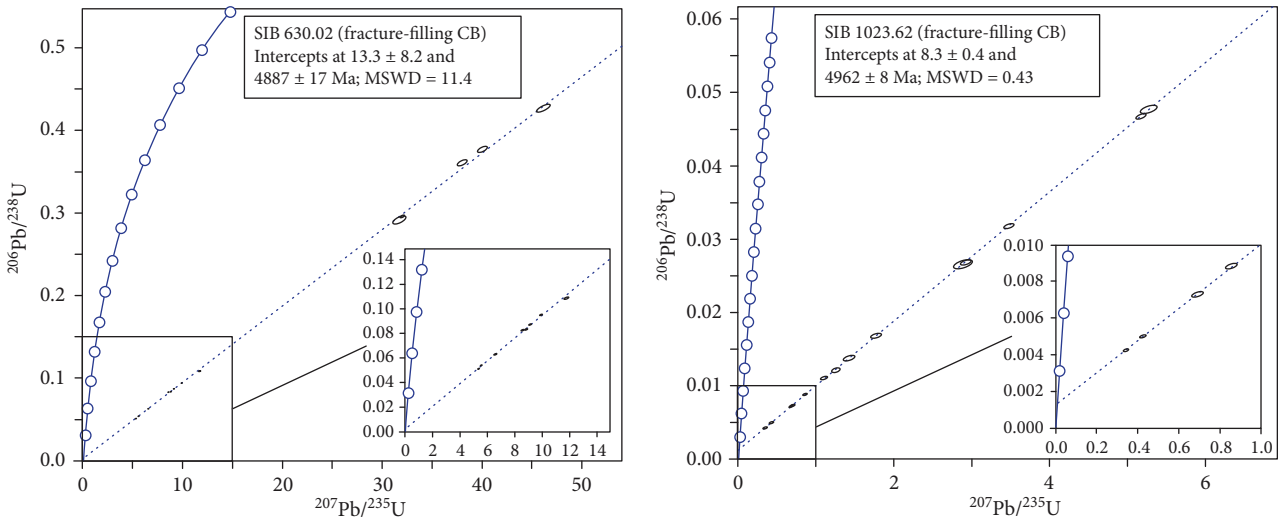

Figure 14: Wetherill concordia diagrams illustrating the results of the LA-ICP-MS analyses of secondary calcites in the Muschelkalk (MK) and the crystalline basement (CB) at the wells of Benken (BEN), Schlattingen (SLA), Siblingen (SIB), and Leuggern (LEU). The error ellipses correspond to two standard deviations of the mean.

simultaneous dissolution of anhydrite and precipitation of quartz. The highly variable salinities of coeval primary fluid inclusions in later calcite at Schafisheim and Bözberg (Figure 10(b)) are interpreted to result from the same mixing process. The saline (~24 wt.% $NaCl_{eq}$) endmember of the mixture was evidently the early postdolomitization pore water. Therefore, it was the low-salinity endmember that infiltrated the dolostones from an external source and triggered dissolution of the anhydrite. Primary fluid inclusions in late calcite in the wells at Benken, Schlattingen, and Siblingen also show variable salinities indicative of mixing, but the values and ranges are much smaller (Figure 10(b)), suggesting that the mixtures were dominated by the dilute endmember. The salinity of the dilute endmember is considered to be equal to that of the least saline of the analysed inclusions at those three wells, namely, 0.2 wt.% $NaCl_{eq.}$.

The secondary saddle dolomites in the deeper wells (Figure 7(h)) contain primary fluid inclusions with smaller but still distinct ranges of salinity between 3.6 and 7.6 wt.% $NaCl_{eq.}$. These ranges may also be due to mixing, but the interpretation is not so obvious as in the cases above. In any case, it is clear that precipitation of the saddle dolomites was triggered by incursion of an external fluid, because their Sr-isotope ratios are much higher than those of the Muschelkalk rock matrix (Figure 8) and because they precipitated at 30–40°C above the temperature of their dolostone wall rocks (Section 4.4). We therefore attribute the precipitation of the saddle dolomites to the same kind of fluid mixing process as recorded by the secondary minerals at shallower wells to the NW.

5.3. Isotope Signatures of the Endmember Fluids. The isotope signatures of the endmember fluids may now be defined to aid tracing of their provenance. Since Sr isotopes do not fractionate at water–mineral equilibrium, the $^{87}Sr/^{86}Sr$ ratio of the saline endmember is assumed to be equal to that of the calcites that precipitated from the high-salinity mixtures in the Muschelkalk at Schafisheim, Böttstein, and Bözberg, i.e., 0.7084–0.7097. These values fall within the range of $^{87}Sr/^{86}Sr$ ratios of the surrounding dolostone matrix (0.7080–0.7106, Figure 8), consistent with our conclusion above that the saline endmember is the inherited pore water in the dolostone. The $\delta^{18}O$ signature of this endmember can be calculated from the isotope composition of the same calcites, since the temperature of water–mineral fractionation is known from the fluid inclusion analyses. The resulting values of ≤4.8‰ VSMOW (Figure 11) identify the pore water as having originally been an evaporative brine, in accord with the likely 3–8‰ range of values outlined in Section 2.3. Such brines typically have high and variable strontium contents of 35–900 mg/L [57].

Using the same approach as above, the isotope signatures of the dilute endmember can be obtained from analyses of the secondary calcites that precipitated from the low-salinity fluid in the Muschelkalk at the Benken and Schlattingen wells. The highest $^{87}Sr/^{86}Sr$ ratio is 0.717 (Figure 8) and the $\delta^{18}O$ values calculated for the parent-water are negative, the lowest value being −7.0‰ VSMOW (Figure 11). The Sr content in the fluid is unknown.

5.4. Provenance of the Dilute Endmember Fluid. According to the hydrogeological evolution of the Muschelkalk outlined in Section 2.3, three scenarios for the provenance of the dilute endmember fluid are conceivable: (1) meteoric runoff from the Black Forest Highlands that laterally infiltrated the Muschelkalk from north to south (Figures 3(c) and 3(d)), (2) infiltration via cross-formational faults from overlying units, and (3) infiltration of formation water via cross-formational faults from underlying units.

Regarding scenario 1, it has been pointed out above that meteoric recharge from the Black Forest Highlands dominates the present-day groundwaters in the Muschelkalk

dolostones. This recharge has high $^{87}Sr/^{86}Sr$ ratios (0.7087–0.7169; Figure 8), whereas its strontium concentration and salinity are rather low (0.02–0.2 mg/L and <0.12 wt.%, respectively [40]). Its $\delta^{18}O$ ratios range from −11.2 to −8.6‰ VSMOW (modern recharge in NE-Jura Mountains and Black Forest Highlands) [20]. Using these data and those of the endmember evaporative brine (with an average Sr concentration of 260 mg/L [57]), mixing trends have been constructed for $\delta^{18}O$ versus $^{87}Sr/^{86}Sr$ ratios (Figure 15(a)) and salinity versus $^{87}Sr/^{86}Sr$ ratios (Figure 15(b)) according to equations in Clark and Fritz [58], p., 105, and Appelo and Postma [59], p. 33. The resulting mixing bands (grey in Figures 15(a) and 15(b)) do not overlap with the low-salinity fluids that precipitated calcite at the Benken and Schlattingen wells, and hence, this mixing scenario cannot account for all the observations at hand. The main argument against the lateral infiltration scenario is the very low strontium concentration in the surface runoff and shallow groundwater from the Black Forest. Thus, rock-water interaction within the sedimentary sequence along the flow path into the Muschelkalk would have readily overprinted the radiogenic basement runoff with a nonradiogenic $^{87}Sr/^{86}Sr$ ratio. Scenario 1 is therefore discarded.

Regarding scenario 2, Figure 8 shows that there is no source of radiogenic strontium in the Keuper–Jurassic units overlying the Muschelkalk that could explain the high $^{87}Sr/^{86}Sr$ ratios of secondary calcite and saddle dolomite at the wells of Benken, Schlattingen, Lindau, and Berlingen. Furthermore, any pore water from the anhydrite-rich Keuper that infiltrated the underlying Muschelkalk would have introduced sulphur with much lower $\delta^{34}S$ values than those observed (Figure 13). Finally, any Keuper water would have been saturated in anhydrite and therefore thermodynamically incapable of dissolving anhydrite nodules in the Muschelkalk. It follows that scenario 2 can be eliminated.

Regarding scenario 3, a possibility is that pore fluid from the immediately underlying Sulfatschichten ascended into the Muschelkalk dolostones. This source can also be discarded, because its pore fluid would have been saturated with respect to halite and anhydrite. Thus, the fluid would have been highly saline rather than dilute, and it would have been unable to dissolve anhydrite nodules in the Muschelkalk. Moreover, since the Sulfatschichten have essentially the same Sr isotope signature as the Muschelkalk (Figure 8), it could not have supplied the highly radiogenic Sr required for the dilute endmember fluid.

Having eliminated the Sulfatschichten, the remaining units underlying the Muschelkalk that are left to consider in scenario 3 are the Buntsandstein, the granite–gneiss basement, and the terrestrial sedimentary rocks in the spatially localized Permocarboniferous troughs. The present-day pore waters in the Permocarboniferous units have oxygen and strontium isotopic signatures that overlap with those of the crystalline basement, and their salinities vary from dilute to locally saline (1–10 wt.% $NaCl_{eq.}$ [20]). Without knowing their age, it is difficult to assess if these waters played a role in the mixing scenario. However, any contribution is likely to have been small, as their very low fluoride and alumina contents [20] cannot explain the pore-filling fluorite and kaolinite in the Muschelkalk. This leaves the Buntsandstein and the granite–gneiss basement, which can be treated as one fluid reservoir: the Buntsandstein has a similar mineralogy to the crystalline rocks because it is their erosional product, and the two units are also known to be hydraulically connected by the same fracture network [60]; hence, it can be assumed that they hosted the same waters. The fluid-inclusion-bearing calcite within fractures in the basement can be used to define the properties of those waters. The early generation of calcite contains old brines (labelled "early" in Figure 10) which are thought to have percolated down from the overlying Sulfatschichten [20, 43] and which cannot have been involved in the mixing process leading to anhydrite dissolution in the Muschelkalk. However, the characteristics of the dilute waters in the late calcite, which also precipitated fluorite and kaolinite, match those of the dilute endmember in the Muschelkalk: salinities are 0.2–6.4 wt.% $NaCl_{eq.}$ (labelled "late" in Figure 10), $\delta^{18}O$ values are between −10.7 and −5.0‰ VSMOW (Figure 11), and $^{87}Sr/^{86}Sr$ ratios are up to 0.717 (Figure 8). The only available indication of the strontium concentration in the water is that of the present-day groundwaters in these units, which range from 0.1 to 16.2 mg/L in the crystalline basement and from 0.7 to 17.8 mg/L in the Buntsandstein [61]. The grey mixing trends for these data in Figures 15(c) and 15(d) overlap with all the assembled constraints, confirming that the low-salinity endmember could have been derived from the underlying basement. Therefore, scenario 3 with the crystalline basement as a fluid source is geochemically the only feasible mixing model among those considered.

As a consistency test, a simple thermodynamic model has been constructed using the software *PhreeqC* [62]. The results (Appendix A.8) show that mixing of a dilute fluid from the basement into the saline brine in the Muschelkalk dolostones will cause spontaneous dissolution of anhydrite and precipitation of secondary calcite and dolomite over a wide range of mixing ratios, consistent with the observations.

5.5. Evidence from Secondary Kaolinite. Derivation of the anhydrite-dissolving endmember fluid from the crystalline basement is further supported by the finding that parent-waters of kaolinite in the Muschelkalk and in the crystalline basement show similar calculated oxygen and hydrogen isotopic signatures (Figure 12). During its geological history, the crystalline basement was affected by several events of hydrothermal alteration, most of which are of Paleozoic age. Only the youngest mineral paragenesis, kaolinite + calcite, postdates the Variscan orogeny but otherwise its age is unconstrained [53]. Kaolinite is present as fracture coatings but also as alteration haloes around the fractures, where it occurs as pseudomorphs after plagioclase. At some wells (e.g., Siblingen), substantial parts of the cored basement section is pervasively kaolinitized and thus this type of alteration may have been widespread. The locally extensive kaolinitic alteration indicates that there must have been huge amounts of fluid circulating through the basement. Accordingly, provided that the basement was hydraulically connected with the Muschelkalk carbonates and a driving force for fluid upwelling was available (see below), it is conceivable that

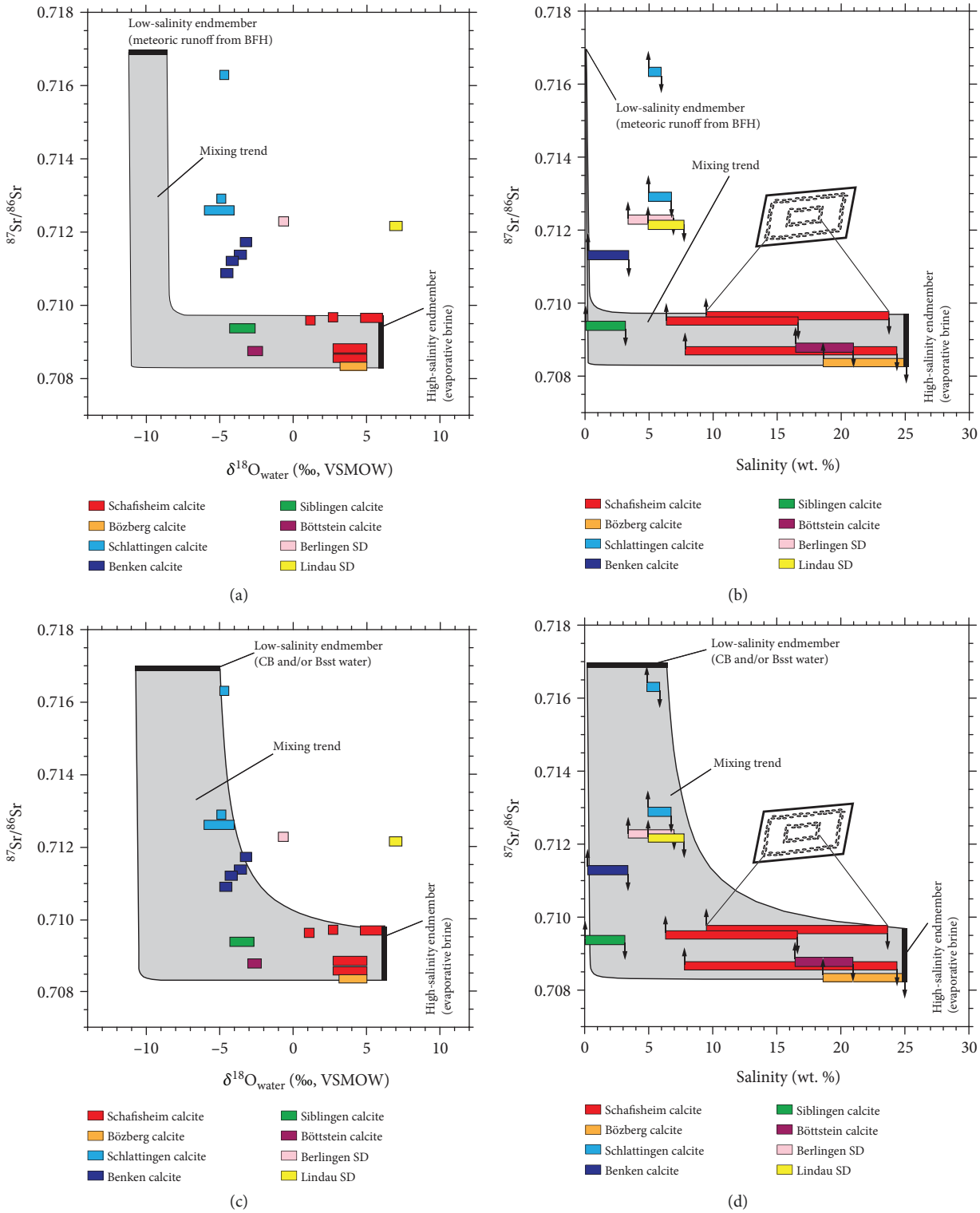

FIGURE 15: (a, c) Calculated $\delta^{18}O$ signatures of calcite and saddle dolomite parent-waters and (b, d) fluid inclusion salinities plotted against corresponding strontium isotope ratios of the secondary calcite and saddle dolomite (SD) in the Muschelkalk. The ranges in fluid inclusion salinity reflect different generations of primary fluid inclusions, whereas the strontium isotope ratio reflects a bulk value. Accordingly, the values at the high salinity end of the horizontal bars are likely to show lower strontium isotope ratios than the values at the low salinity end of the bars (black arrows). The grey areas represent mixing trends calculated for two infiltration scenarios outlined in Section 2.3 and 5.: (a, b) recharge of meteoric runoff in the Black Forest Highlands (BFH) and lateral infiltration of the Muschelkalk in the Swiss Molasse Basin and (c, d) infiltration of deep groundwater from the Buntsandstein (Bsst) and/or the crystalline basement (CB) via fluid ascent along faults or fractures (Figure 5).

these basement waters could have infiltrated the Muschelkalk carbonates, triggered anhydrite dissolution, and precipitated secondary minerals. According to Mazurek [53], kaolinitic alteration in the crystalline basement is present at the wells of Böttstein, Leuggern, Kaisten, Siblingen, Pfaffnau, and Herdern (no meaningful information is available for the wells at Benken and Schlattingen). Apart from the Pfaffnau well, the geographic occurrence of kaolinitic alteration in the crystalline basement correlates well with the geographic occurrence of complete anhydrite dissolution in the Muschelkalk dolostones (Figure 5). This correlation is taken as further support for the scenario of basement-derived fluid having dissolved the anhydrite nodules.

5.6. Age and Temperature Constraints on Fluid Mixing and Anhydrite Dissolution. The U–Pb ages of the calcites that postdate anhydrite dissolution in the Muschelkalk at the wells of Schlattingen, Benken, Siblingen, and Leuggern lie between 11.5 ± 0.5 and 16.8 ± 4.0 Ma (Figures 14(a)–14(f)), indicating precipitation of calcite ± kaolinite in the anhydrite moulds during the Early–Middle Miocene. This age constraint is another argument against lateral infiltration of meteoric runoff from the Black Forest Highlands, as that scenario requires that both the Triassic Muschelkalk and the crystalline basement were exhumed at the time of infiltration. Exhumation of the Muschelkalk is required to provide outcrops to recharge freshwater, whereas exhumation of the basement is required to provide meteoric runoff that acquired high strontium isotope ratios by interacting with the Variscan granites and gneisses. According to the erosional history of the Black Forest Highlands, which is recorded by the deposition of the Younger Juranagelfluh conglomerates, exhumation of the basement occurred at around 10 Ma [63], somewhat later than the precipitation of secondary calcite in the Muschelkalk dolostones.

At Benken and Schlattingen, the rock temperature in the Muschelkalk dolostones was ~52–67°C during the 11.5–16.8 Ma period of secondary calcite deposition (Figure 2), some 25°C cooler than the fluid that precipitated the calcite (Figure 10). This is compatible with the scenario that the parent fluid of the calcite ascended from the hotter basement, but it seems impossible to explain by the scenario of lateral infiltration of freshwater from the Black Forest Highlands.

5.7. Paths, Driving Forces, and Timing of Fluid Migration. The calcite ages of 11.5–16.8 Ma correspond to a time of large-scale updoming of the Black Forest Highlands and subsidence of the Molasse Basin (Section 2.2; Figure 3). These events were accompanied by extensional tectonics in the upper crust that reactivated old, Paleozoic structures in the basement and that induced new faults and flexures in the Mesozoic sediments of the northeastern SMB (Section 2.2). Figure 5 shows the large number of faults that link the basement with the overlying Triassic units, many of which also rise up through the top of the Upper Muschelkalk. All of these faults could have acted as fluid pathways between the Variscan basement and the overlying Muschelkalk. Moreover, the newly established hydraulic gradients that resulted from the updoming of the Black Forest Highlands in the NW would have provided a driving force to mobilize groundwaters residing in the fracture network within the basement and Buntsandstein. Thus, these fluids could have been forced upwards along faults into the Muschelkalk. A critical point in this scenario is the need for exfiltration areas in the Muschelkalk to establish through-flow. There is evidence of fluvial erosion in the Mesozoic sediments along the southern flank of the Black Forest Highlands during Miocene times [15, 63]. However, it is unclear whether this erosion cut deeply enough into the Muschelkalk to create exfiltration pathways.

Secondary quartz is shown in Section 4.1 to have precipitated during anhydrite dissolution. At Benken and Schlattingen, this precipitation occurred at 41–58°C (Figure 10 and Table A.3). When plotted onto the temperature–time curve for the Benken area (Figure 2), these precipitation temperatures indicate an Oligocene age for anhydrite dissolution, a period during which extensional tectonics and cross-formational faulting began in the northeastern SMB. The age of saddle dolomite cementation in the eastern wells is not known, but assuming it also formed during the Oligocene, it can be expected that the occurrence of anhydrite-dissolution porosity in the entire Benken–Schlattingen–Berlingen–Lindau region was controlled by the occurrence of faults and fractures that hydraulically connected the crystalline basement with the overlying Muschelkalk.

In addition to all the above evidence from the SMB, there is also evidence that basement fluids have been mobilized since the end of the Oligocene in the Black Forest Highlands themselves. There, Jurassic/Tertiary Pb–Zn–fluorite–quartz–barite veins contain late-stage hydrothermal (~20–70°C) minerals including calcite, dolomite, siderite and Ca-sulphates [64]. Dating of these carbonates by the U–Pb method yielded robust ages between 20 and 0.6 Ma, which Burisch et al. [64] correlated with uplift and rifting of the basement along the Rhine graben (Figures 1 and 3). Mineral parageneses of secondary quartz, calcite, barite, fluorite, and minor ore minerals are also found in the crystalline basement of the SMB, and our U–Pb dating of two calcites in basement fractures at Siblingen yields ages of 8.3 ± 0.5 and 13.3 ± 8.2 Ma (Figures 14(g) and 14(h), respectively). These values match the timing of calcite precipitation in the Black Forest Highlands. Furthermore, within the uncertainty of the age determination, the 13.3 Ma basement sample matches the ages of the secondary calcites in the Muschelkalk (11.5–16.8 Ma), although the 8.3 Ma sample is distinctly younger.

While the geochemical evidence for structurally controlled infiltration of basement water into the overlying Muschelkalk is compelling, only faults with large offsets would be able to juxtapose basement and the Muschelkalk dolostones and bypass the intervening halite-bearing Sulfatschichten. Otherwise, as argued in Section 5.4, contact of the basement fluid with the Sulfatschichten would increase salinity, saturate the solution in anhydrite, and lower the $^{87}Sr/^{86}Sr$ ratio, all in contradiction to the observations. Accordingly, fluid ascent from the basement must have occurred along faults that displaced the stratigraphy by >100 m, such that the fractured basement was directly in

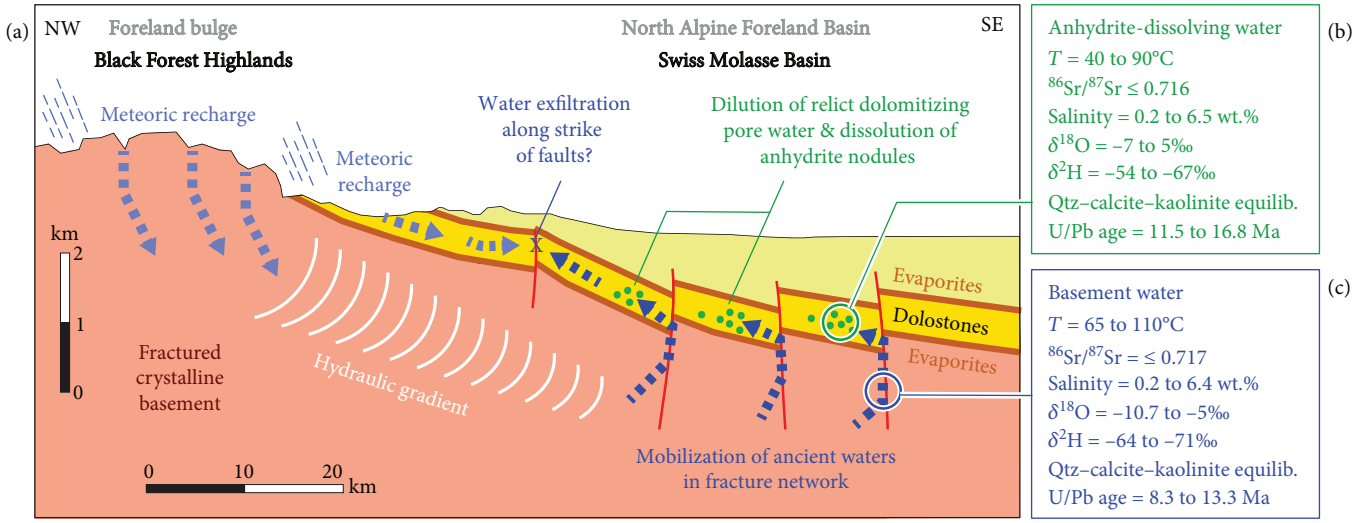

Figure 16: (a) Schematic geological cross section illustrating upwelling basement water leading to anhydrite dissolution and generation of secondary porosity in the Muschelkalk dolostones (note vertical exaggeration; see text for details). (b) Properties of anhydrite-dissolving fluid deduced from evidence within dolostones. (c) Matching properties of pore water deduced from evidence in basement veins.

contact with the dolostones. Numerous fault segments that satisfy these conditions occur in the areas of anhydrite dissolution shown in Figure 5 (an example is given in Figure A.9); thus, it appears that flow paths that circumvent the Sulfatschichten were indeed available. Figure 16 schematically illustrates the deduced infiltration of basement fluid into the Upper Muschelkalk.

The partial to complete removal of anhydrite from the dolostones over an area of >55 km^2 (Figure 5(a)) implies that large amounts of basement fluid infiltrated the Muschelkalk. The resulting mixture of basement water and relict dolomitizing brine evidently remained in the Muschelkalk dolostones through to today, as evidenced by the more saline NaCl-dominated waters in the deeper wells of the SMB [21, 22]. During the Pleistocene, these saline waters were in turn diluted by infiltration of meteoric water from the Black Forest Highlands directly into the exposed Muschelkalk, yielding the compositional variety in groundwaters now found in the NE of the SMB (Section 2.3).

6. Conclusions

Several sources of geochemical evidence (petrography, stable and radiogenic isotopes, fluid inclusion analyses, and radiometric ages) have been integrated to identify the process and timing of the anhydrite dissolution that enhanced porosity in the Muschelkalk dolostones. All these lines of evidence point to incursion of rock-equilibrated groundwater from the underlying crystalline basement and/or the Buntsandstein as the trigger for anhydrite dissolution. The fluids presumably ascended along the numerous known preexisting Paleozoic faults, which were reactivated by Oligocene–Miocene extensional tectonics in the upper crust. The concurrent subsidence of the Molasse Basin and updoming of the Black Forest Highlands to the north of the Basin generated hydraulic gradients that drove fluid through the fractured basement and up into the Muschelkalk (Figure 16). It follows that anhydrite-dissolution porosity in the Muschelkalk dolostones is likely to be spatially restricted to areas which are both (1) on the downthrown side of basement-cover cross-formationalfaults (e.g., Figure 16) and (2) subjected to the hydraulic gradient from the Black Forest Highlands (Figure 16).

Thus, this study has shown that the porosity of dolostones can be significantly enhanced (e.g., gain of up to 15 vol.%) in the deep mesogenetic setting (700–2300 m depth at 40–160°C) by areally extensive (> 55 km^2) dissolution of eogenetic anhydrite. Similar effects can be expected in the foreland basins of other continent–continent collision belts, where anhydrite-bearing dolostones have been inherited from the pre-orogenic history. In such settings, the critical factors that must coincide to generate secondary porosity via anhydrite dissolution are the following: (1) the rocks in the foreland bulge must be exposed subaerially to establish a hydraulic head gradient versus the rocks buried in the adjacent basin; (2) the exposed rocks must contain permeable fracture networks or other aquifers that connect to permeable cross-formational structures intersecting the dolostones deep in the basin; and (3) the fluids that are thereby forced up into the dolostones must be undersaturated with respect to anhydrite.

Data Availability

The data used to support the findings of this study are included within the supplementary information file.

Disclosure

The abstract of this manuscript has been submitted for presentation at the 16th Swiss Geoscience Meeting, Bern 2018 (1st December).

Conflicts of Interest

The authors declare that there is no conflict of interest regarding the publication of this paper.

Acknowledgments

This research was conducted within the framework of the Swiss Competence Center for Energy Research – Supply of Energy (SCCER-SoE), with support of the Swiss National Science Foundation (SNSF) via NRP70 "Energy Turnaround" (Grant 407040_153889 to L.W.D). We thank the Swiss National Cooperative for the Disposal of Radioactive Waste (Nagra) and the Corporation for Swiss Petroleum (SEAG) for generously granting access to their drill cores and wireline logs. The Swiss Federal Office of Topography swisstopo provided data from their GeoMol digital subsurface model, from which Daniel Egli kindly deduced fault traces and offsets in the Muschelkalk. We appreciate discussions with Arthur Adams and Daniel Traber.

Supplementary Materials

A1: Table A.1: depth and thickness of the Trigonodus Dolomit and the Dolomit der Anhydritgruppe at all the wells investigated in this study. A2: Table A.2: strontium isotope data for minerals and groundwater from various wells across the Swiss Molasse Basin. A3: Table A.3: compilation of microthermometric analyses of primary fluid inclusions in secondary minerals from various wells across the Swiss Molasse Basin. A4: Table A.4: results of the oxygen isotope analyses and calculated parent-waters of secondary quartz, calcite, and dolomite from various wells across the Swiss Molasse Basin. A5: Table A.5: results of the oxygen and hydrogen isotope analyses of secondary kaolinite and calculated parent-waters from various wells across the Swiss Molasse Basin. A6: Table A.6: results of the sulphur isotope analyses of anhydrite nodules and secondary pore- and fracture-filling anhydrite in the Muschelkalk and the overlying Keuper. A7: Table A.7: results of the LA-ICP-MS analyses of secondary calcites from the wells at Benken, Schlattingen, Siblingen, and Leuggern. A8: PhreeqC modelling of groundwater mixing A9: Figure A.9: infiltration pathway of upwelling basement water. *(Supplementary Materials)*

References

[1] M. W. Longman, "Carbonate diagenetic textures from near-surface diagenetic environments," *AAPG Bulletin*, vol. 64, pp. 461–487, 1980.

[2] N. P. James and P. W. Choquette, "Diagenesis 9. Limestones–the meteoric diagenetic environment," *Geoscience Canada*, vol. 11, pp. 161–194, 1984.

[3] P. W. Choquette and N. P. James, "Diagenesis 12: Diagenesis in limestones: 3. The deep burial environment," *Geoscience Canada*, vol. 14, pp. 3–35, 1987.

[4] J. Jameson, "Models of porosity formation and their impact on reservoir description, Lisburne field, Prudhoe Bay, Alaska," *AAPG Bulletin*, vol. 78, pp. 1651–1678, 1994.

[5] E. C. Heasley, R. H. Worden, and J. P. Hendry, "Cement distribution in a carbonate reservoir: recognition of a palaeo oil–water contact and its relationship to reservoir quality in the Humbly Grove field, onshore, UK," *Marine and Petroleum Geology*, vol. 17, no. 5, pp. 639–654, 2000.

[6] A. P. Heward, S. Chuenbunchom, G. Makel, D. Marsland, and L. Spring, "Nang Nuan oil field, B6/27, Gulf of Thailand: karst reservoirs of meteoric or deep-burial origin?," *Petroleum Geoscience*, vol. 6, no. 1, pp. 15–27, 2000.

[7] S. N. Ehrenberg, O. Walderhaug, and K. Bjorlykke, "Carbonate porosity creation by mesogenetic dissolution: reality or illusion?," *AAPG Bulletin*, vol. 96, no. 2, pp. 217–233, 2012.

[8] O. A. Pfiffner, P. F. Erard, and M. Stäuble, "Two cross sections through the Swiss Molasse basin (lines E4-E6, W1, W7-W10)," in *Results of NRP 20- Deep Structure of the Swiss Alps*, O. A. Pfiffner, P. Lehner, P. Heitzmann, S. Müller, and A. Steck, Eds., pp. 64–72, Birkhäuser, Basel, Switzerland, 1997.

[9] Nagra, *Projekt Opalinuston: Synthese der geowissenschaftlichen Untersuchungsergebnisse*, Nagra Technischer Bericht NTB 02–03, Nagra, Wettingen, Switzerland, 2002.

[10] G. Chevalier, L. W. Diamond, and W. Leu, "Potential for deep geological sequestration of CO_2 in Switzerland: a first appraisal," *Swiss Journal of Geosciences*, vol. 103, no. 3, pp. 427–455, 2010.

[11] O. A. Pfiffner, *Geology of the Alps*, John Wiley & Sons, 2014.

[12] M. Thury, A. Gautschi, M. Mazurek et al., *Geology and Hydrogeology of the Crystalline Basement of Northern Switzerland: Synthesis of Regional Investigations 1981–1993 within the Nagra Radioactive Waste Disposal Programme*, Nagra Technical Report NTB 93–01, Nagra, Wettingen, Switzerland, 1994.

[13] M. Mazurek, A. J. Hurford, and W. Leu, "Unravelling the multi-stage burial history of the Swiss Molasse Basin: integration of apatite fission track, vitrinite reflectance and biomarker isomerisation analysis," *Basin Research*, vol. 18, no. 1, pp. 27–50, 2006.

[14] H. Naef, P. Birkhäuser, and P. Roth, *Interpretation der Reflexionsseismik im Gebiet nördlich Lägeren–Zürcher Weinland*, Nagra Technischer Bericht NTB 94–14, Nagra, Wettingen, Switzerland, 1995.

[15] W. H. Müller, H. Naef, and H. R. Graf, *Geologische Entwicklung der Nordschweiz, Neotektonik und Langzeitszenarien Zürcher Weinland*, Nagra Technischer Bericht NTB 99–08, Nagra, Wettingen, Switzerland, 2002.

[16] M. Schauer and T. Aigner, "Cycle stacking pattern, diagenesis and reservoir geology of peritidal dolostones, Trigonodus-Dolomite, Upper Muschelkalk (Middle Triassic, SW-Germany)," *Facies*, vol. 37, no. 1, pp. 99–113, 1997.

[17] A. Adams and L. W. Diamond, "Early diagenesis driven by widespread meteoric infiltration of a Central European carbonate ramp: a reinterpretation of the Upper Muschelkalk," *Sedimentary Geology*, vol. 362, pp. 37–52, 2017.

[18] A. Adams, L. W. Diamond, and L. Aschwanden, "Dolomitization by hypersaline reflux into dense groundwaters as revealed by vertical trends in strontium and oxygen isotopes: Upper Muschelkalk, Switzerland," *Sedimentology*, vol. 66, pp. 362–390, 2019.

[19] J. A. McKenzie, K. J. Hsü, and J. F. Schneider, "Movement of subsurface waters under the sabkha, Abu Dhabi, UAE, and its relation to evaporative dolomite genesis," in *Concepts and models of Dolomitization*, D. H. Zenger, J. B. Dunham, and

R. L. Ethington, Eds., vol. 28, pp. 11–30, Society for Sedimentary Geology, 1980.

[20] F. J. Pearson, W. Balderer, H. H. Loosli et al., *Applied Isotope Hydrogeology – a Case Study in Northern Switzerland*, Elsevier, Amsterdam, Netherlands, 1991.

[21] H. N. Waber, M. Heidinger, G. Lorenz, and D. Traber, *Hydrochemie und Isotopenhydrogeologie von Tiefengrundwässern in der Nordschweiz und im angrenzenden Süddeutschland*, Nagra Arbeitsbericht NAB 13–63, Nagra, Wettingen, Switzerland, 2014.

[22] D. Biehler, H. Schmassmann, K. Schneemann, and J. Sillanpää, *Hydrochemische Synthese Nordschweiz: Dogger-, Lias-, Keuper- und Muschelkalk-Aquifere*, Nagra Technischer Bericht NTB 92–08, Nagra, Wettingen, Switzerland, 1993.

[23] P. Birkhäuser, P. Roth, B. Meier, and H. Naef, *3D-Seismik: Räumliche Erkundung der mesozoischen Sedimentschichten im Zürcher Weinland*, Nagra Technischer Bericht NTB 00–03, Nagra, Wettingen, Switzerland, 2001.

[24] A. Sommaruga, U. Eichenberger, and F. Marillier, *Seismic Atlas of the Swiss Molasse Basin*, Swiss Federal Office of Topography Swisstopo, Wabern, 2012.

[25] L. W. Diamond and D. D. Marshall, "Evaluation of the fluid-inclusion crushing-stage as an aid in exploration for mesothermal gold-quartz deposits," *Journal of Geochemical Exploration*, vol. 38, no. 3, pp. 285–297, 1990.

[26] Z. D. Sharp, "A laser-based microanalytical method for the in situ determination of oxygen isotope ratios of silicates and oxides," *Geochimica et Cosmochimica Acta*, vol. 54, no. 5, pp. 1353–1357, 1990.

[27] A. E. Fallick, C. I. Macaulay, and R. S. Haszeldine, "Implications of linearly correlated oxygen and hydrogen isotopic compositions for kaolinite and illite in the Magnus Sandstone, North Sea," *Clays and Clay Minerals*, vol. 41, no. 2, pp. 184–190, 1993.

[28] S. Kasemann, A. Meixner, A. Rocholl et al., "Boron and oxygen isotope composition of certified reference materials NIST SRM 610/612 and reference materials JB-2 and JR-2," *Geostandards and Geoanalytical Research*, vol. 25, no. 2-3, pp. 405–416, 2001.

[29] A. Tarantola, J. Mullis, T. Vennemann, J. Dubessy, and C. De Capitani, "Oxidation of methane at the CH_4/H_2O–(CO_2) transition zone in the external part of the Central Alps, Switzerland: evidence from stable isotope investigations," *Chemical Geology*, vol. 237, no. 3-4, pp. 329–357, 2007.

[30] A.-L. Jourdan, T. W. Vennemann, J. Mullis, and K. Ramseyer, "Oxygen isotope sector zoning in natural hydrothermal quartz," *Mineralogical Magazine*, vol. 73, no. 4, pp. 615–632, 2009.

[31] C. Spötl and T. W. Vennemann, "Continuous-flow isotope ratio mass spectrometric analysis of carbonate minerals," *Rapid Communications in Mass Spectrometry*, vol. 17, no. 9, pp. 1004–1006, 2003.

[32] A. Krabbenhöft, J. Fietzke, A. Eisenhauer, V. Liebetrau, F. Böhm, and H. Vollstaedt, "Determination of radiogenic and stable strontium isotope ratios ($^{87}Sr/^{86}Sr$; $\delta^{88}/^{86}Sr$) by thermal ionization mass spectrometry applying an $^{87}Sr/^{84}Sr$ double spike," *Journal of Analytical Atomic Spectrometry*, vol. 24, no. 9, pp. 1267–1271, 2009.

[33] J. E. Spangenberg, J. V. Lavrič, N. Meisser, and V. Serneels, "Sulfur isotope analysis of cinnabar from Roman wall paintings by elemental analysis/isotope ratio mass spectrometry - tracking the origin of archaeological red pigments and their authenticity," *Rapid Communications in Mass Spectrometry*, vol. 24, no. 19, pp. 2812–2816, 2010.

[34] D. W. Davis, *Application of U-Pb Geochronology Methods to the Absolute Age Determination of Secondary Calcite*, Report no. NWMO-TR-2013-21. Nuclear Waste Management Organization, Toronto, Canada, 2013.

[35] D. W. Davis, *Continued Application of U-Pb Geochronology Methods to the Absolute Age Determination of Secondary Calcite: 2014-2016*, Report no. NWMO-TR-2016-07. Nuclear Waste Management Organization, Toronto, Canada, 2016.

[36] L. Aschwanden, L. W. Diamond, and A. Adams, "Effects of progressive burial on matrix porosity and permeability of dolostones in the foreland basin of the Alpine Orogen, Switzerland," *Marine and Petroleum Geology*, vol. 100, pp. 148–164, 2019.

[37] A. Matter, T. Peters, and K. Ramseyer, "$^{87}Sr/^{86}Sr$-Verhältnisse und Sr-Gehalte von Tiefengrundwässern, Mineralien sowie Gesteinen us dem Kristallin und der Trias der Nordschweiz," *Eclogae Geologicae Helvetiae*, vol. 80, pp. 579–592, 1987.

[38] Nagra, *Sondierbohrung Benken–Untersuchungsbericht*, Nagra Technischer Bericht NTB 00–01, Nagra, Wettingen, Switzerland, 2001.

[39] J. M. McArthur, R. J. Howarth, and T. R. Bailey, "Strontium isotope stratigraphy: LOWESS version 3: best fit to the marine Sr-isotope curve for 0–509 Ma and accompanying look-up table for deriving numerical age," *Journal of Geology*, vol. 109, no. 2, pp. 155–170, 2001.

[40] S. Durand, F. Chabaux, S. Rihs, P. Duringer, and P. Elsass, "U isotope ratios as tracers of groundwater inputs into surface waters: example of the Upper Rhine hydrosystem," *Chemical Geology*, vol. 220, no. 1-2, pp. 1–19, 2005.

[41] L. W. Diamond, "Systematics of H_2O inclusions," in *Short Course 32- Fluid Inclusions: Analysis and Interpretation*, I. M. Samson, A. J. Anderson, and D. D. Marshall, Eds., pp. 55–79, Mineralogical Association of Canada, 2003.

[42] L. W. Diamond, "Introduction to gas-bearing aqueous fluid inclusions," in *Short Course 32- Fluid Inclusions: Analysis and Interpretation*, I. M. Samson, A. J. Anderson, and D. D. Marshall, Eds., pp. 101–158, Mineralogical Association of Canada, 2003.

[43] J. Mullis, "Fluideinschluss-Untersuchungen in den Nagra-Bohrungen der Nordschweiz," *Eclogae Geologicae Helvetiae*, vol. 80, pp. 553–568, 1987.

[44] D. L. Hall, S. M. Sterner, and R. J. Bodnar, "Freezing point depression of NaCl-KCl-H_2O solutions," *Economic Geology*, vol. 83, no. 1, pp. 197–202, 1988.

[45] A. Matter, T. Peters, H. R. Bläsi, F. Schenker, and H. P. Weiss, *Sondierbohrung Schafisheim: Geologie*, Nagra Technischer Bericht NTB 86–03, Nagra, Wettingen, Switzerland, 1988.

[46] T. Peters, A. Matter, J. Meyer, C. Isenschmid, and H. J. Ziegler, *Sondierbohrung Kaisten: Geologie*, Nagra Technischer Bericht NTB 86–04, Nagra, Wettingen, Switzerland, 1989.

[47] T. Peters, A. Matter, H. R. Bläsi et al., *Sondierbohrung Leuggern: Geologie*, Nagra Technischer Bericht NTB 86–05, Nagra, Wettingen, Switzerland, 1989.

[48] I. Friedman and J. R. O'Neil, *Compilation of Stable Isotope Fractionation Factors of Geochemical Interest*, U.S. Geological Survey Professional Paper 440-KK, 1977.

[49] Z. Yong-Fei, "Calculation of oxygen isotope fractionation in anhydrous silicate minerals," *Geochimica et Cosmochimica Acta*, vol. 57, no. 5, pp. 1079–1091, 1993.

[50] Nagra, *Sondierbohrung Kaisten Untersuchungsbericht*, Nagra Technischer Bericht NTB 88–12, Nagra, Wettingen, Switzerland, 1991.

[51] Nagra, *Sondierbohrung Siblingen Untersuchungsbericht*, Nagra Technischer Bericht NTB 90–34, Nagra, Wettingen, Switzerland, 1992.

[52] S. M. F. Sheppard and H. A. Gilg, "Stable isotope geochemistry of clay minerals," *Clay Minerals*, vol. 31, no. 01, pp. 1–24, 1996.

[53] M. Mazurek, *Geology of the Crystalline Basement of Northern Switzerland and Derivation of Geological Input Data for Safety Assessment Models*, Nagra Technical Report NTB 93–12, Nagra, Wettingen, Switzerland, 1998.

[54] Y. Yurtsever and J. R. Gat, "Atmospheric water," in *Stable Isotope Hydrogeology: Deuterium and Oxygen-18 in the Water Cycle*, Technical Report Series 201. IAEA, Vienna, Austria, 1981.

[55] M. Kullin and H. Schmassmann, "Isotope composition of modern recharge," in *Applied Isotope Hydrogeology - a Case Study in Northern Switzerland*, F. J. Pearson, W. Balderer, H. H. Loosli, B. E. Lehmann, A. Matter, T. Peters, H. Schmassmann, and A. Gautschi, Eds., pp. 65–90, Elsevier, Amsterdam, Netherlands, 1991.

[56] S. M. Bernasconi, I. Meier, S. Wohlwend et al., "An evaporite-based high-resolution sulfur isotope record of Late Permian and Triassic seawater sulfate," *Geochimica et Cosmochimica Acta*, vol. 204, pp. 331–349, 2017.

[57] W. W. Wood, W. E. Sanford, and S. K. Frape, "Chemical openness and potential for misinterpretation of the solute environment of coastal sabkhat," *Chemical Geology*, vol. 215, no. 1-4, pp. 361–372, 2005.

[58] I. Clark and P. Fritz, *Environmental Isotopes in Hydrogeology*, Lewis Publishers, Boca Raton, FL, USA, 1997.

[59] C. A. J. Appelo and D. Postma, *Geochemistry, Groundwater and Pollution*, A.A. Balkema, Rotterdam, Netherlands, 2nd edition, 2007.

[60] H. Schmassmann, M. Kullin, and K. Schneemann, *Hydrochemische Synthese Nordschweiz: Buntsandstein-, Perm-, und Kristallin-Aquifere*, Nagra Technischer Bericht NTB 91–30, Nagra, Wettingen, Switzerland, 1992.

[61] C. Wittwer, *Probenahmen und chemische Analysen von Grundwässern aus den Sondierbohrungen*, Nagra Technischer Bericht NTB 85–49, Nagra, Wettingen, Switzerland, 1986.

[62] D. L. Parkhurst and C. A. J. Appelo, *User's Guide to PHREEQC (Version 2) - a Computer Program for Speciation, Batch-Reaction, One-Dimensional Transport, and Inverse Geochemical Calculations*, Water-Resources Investigations Report 99–4259. US Geological Survey, Denver, CO, USA, 1999.

[63] F. Hofmann, "Zur plio-pleistozänen Landschaftsgeschichte im Gebiet Hochrhein-Wutach-Randen-Donau: Geomorphologische Überlegungen und sedimentpetrographische Befunde," *Eclogae Geologicae Helvetiae*, vol. 89, pp. 1023–1041, 1996.

[64] M. Burisch, B. F. Walter, A. Gerdes, M. Lanz, and G. Markl, "Late-stage anhydrite-gypsum-siderite-dolomite-calcite assemblages record the transition from a deep to a shallow hydrothermal system in the Schwarzwald mining district, SW Germany," *Geochimica et Cosmochimica Acta*, vol. 223, pp. 259–278, 2018.